

On Kinematic Measurements of Self-Gravity in Protoplanetary Disks

SEAN M. ANDREWS ¹ RICHARD TEAGUE ² CHRISTOPHER P. WIRTH ^{1,3} JANE HUANG ^{4,5} AND ZHAOHUAN ZHU ^{6,7}

¹Center for Astrophysics | Harvard & Smithsonian, 60 Garden Street, Cambridge, MA 02138, USA

²Department of Earth, Atmospheric, and Planetary Sciences, Massachusetts Institute of Technology, Cambridge, MA 02139, USA

³Department of Astronomy & Astrophysics, University of Chicago, 5640 S. Ellis Avenue, Chicago, IL 60637, USA

⁴Department of Astronomy, University of Michigan, 323 West Hall, 1085 S. University Avenue, Ann Arbor, MI 48109, USA

⁵Department of Astronomy, Columbia University, Mail Code 5246, 538 West 120th Street, New York, NY 10027, USA

⁶Department of Physics and Astronomy, University of Nevada, Las Vegas, 4505 South Maryland Parkway, Las Vegas, NV 89154, USA

⁷Nevada Center for Astrophysics, University of Nevada, Las Vegas, 4505 South Maryland Parkway, Las Vegas, NV 89154, USA

ABSTRACT

Using controlled injection and recovery experiments, we devised an analysis prescription to assess the quality of dynamical measurements of protoplanetary disk gas masses based on resolved (CO) spectral line data, given observational limitations (resolution, sampling, noise), measurement bias, and ambiguities in the geometry and physical conditions. With sufficient data quality, this approach performed well for massive disks ($M_d/M_* = 0.1$): we inferred M_d posteriors that recovered the true values with little bias ($\lesssim 20\%$) and uncertainties within a factor of two (2σ). The gas surface density profiles for such cases are recovered with remarkable fidelity. Some experimentation indicates that this approach becomes insensitive when $M_d/M_* \lesssim 5\%$, due primarily to degeneracies in the surface density profile parameters. Including multiple lines that probe different vertical layers, along with some improvements in the associated tools, might push that practical boundary down by another factor of \sim two in ideal scenarios. We also demonstrated this analysis approach using archival ALMA observations of the MWC 480 disk (Öberg et al. 2021): we measured $M_d = 0.13^{+0.04}_{-0.01} M_\odot$ (corresponding to $M_d/M_* = 7 \pm 1\%$) and identified kinematic substructures consistent with surface density gaps around 65 and 135 au. Overall, this (and similar work) suggests that these dynamical measurements offer powerful new constraints with sufficient accuracy and precision to quantify gas masses and surface densities at the high end of the M_d/M_* distribution, and therefore can serve as key benchmarks for detailed thermo-chemical modeling. We address some prospects for improvements, and discuss various caveats and limitations to guide future work.

1. INTRODUCTION

The masses of circumstellar disks are fundamental inputs for all models of planet formation. The amount of disk material regulates evolution in its structure, which in turn sets key planetary growth efficiencies and drives the early dynamics of planetary systems. But disk mass (M_d) measurements are challenging. The dominant constituent (cold H₂ gas) is inaccessible to observations, and our confidence in the assumed conversions or extrapolations from indirect proxies is limited (Bergin & Williams 2018; Andrews 2020; Miotello et al. 2023).

The most common M_d estimates are based on the dust continuum emission at millimeter wavelengths. If that emission is optically thin, the luminosity is directly proportional to the dust mass (Beckwith et al. 1990). The key uncertainties in such conversions are temperatures, opacities, and dust-to-gas ratios: the latter two factors could span large ranges depending on the evolutionary state (Birnstiel et al. 2012, 2016; Testi et al. 2014) and microphysical properties (Ossenkopf & Henning 1994;

Birnstiel et al. 2018) of the dust. The typical assumptions – a simple temperature profile and spatially uniform opacity and dust-to-gas ratio, with particle sizes that maximize the opacity – favor *minimal* masses (e.g., Liu et al. 2022). In general, an appreciable fraction of the emission is optically thick (e.g., Andrews & Williams 2005), and localized dust over-densities can further bloat the optical depths (Ricci et al. 2012; ALMA Partnership et al. 2015; Huang et al. 2018a). This reinforces that M_d constraints are lower bounds, since high optical depths hide mass. Such M_d underestimates can be severe if the dust albedos are high (Zhu et al. 2019).

Although more of an observational challenge, resolved measurements of spectral line intensities offer a more direct probe of the gas reservoir. The most common diagnostics for estimating M_d are pure rotational transitions from CO isotopologues (Williams & Best 2014; Miotello et al. 2014, 2016; Zhang et al. 2017). These constraints have analogous systematics to the dust continuum, most significantly due to ambiguities in the molecular abun-

dances relative to H₂ (Aikawa et al. 1996; Dutrey et al. 1997; van Zadelhoff et al. 2001; Miotello et al. 2017; Yu et al. 2017; Schwarz et al. 2018; Krijt et al. 2020) and high optical depths (Booth et al. 2019). The far-infrared HD transitions are appealing alternatives (but currently inaccessible), since the D/H ratio is better understood (Bergin et al. 2013; McClure et al. 2016; Trapman et al. 2017). But as with CO, M_d estimates from HD require extrapolations in optical depths, temperatures, vertical structure, and factors that set the local continuum.

The emerging consensus is that more robust M_d estimates are accessible by self-consistently modeling a combination of diagnostics, for the dust (multifrequency resolved continuum; e.g., Carrasco-González et al. 2019; Macías et al. 2021; Sierra et al. 2021) and the gas (resolved groupings of key spectral lines; e.g., Schwarz et al. 2016, 2021; Molyarova et al. 2017; Zhang et al. 2017, 2021; Anderson et al. 2019, 2022; Trapman et al. 2022). However, all of these approaches depend on interpreting continuum or line intensities, and are therefore subject to the ambiguities associated with conversion factors from emission to physical conditions and prone to underestimating M_d (especially for high values) because material is hidden by high optical depths.

A compelling and complementary alternative for gas masses is available in the *kinematic* information of spectral line data, through the velocity deviations induced by self-gravity (Rosenfeld et al. 2013). The disk potential increases the gas disk orbital velocities relative to the rate expected from the stellar potential alone, because the total encircled mass is always higher than the stellar mass M_* . Though these kinematic signatures are subtle, their interpretation does not rely on line *intensities*: systematics associated with conversion factors and optical depths are minimal. This dynamical method is a new opportunity for accurate M_d measurements, particularly at high values. Veronesi et al. (2021) made the first such measurement, based on Atacama Large Millimeter/submillimeter Array (ALMA) data for the Elias 27 disk. Lodato et al. (2023) and Martire et al. (2024) then followed up with measurements for the disks in the MAPS project sample (Öberg et al. 2021).

These pioneering studies demonstrate the potential of this new, dynamical approach for measuring M_d . But the observational features are subtle, and measurements are fickle: some challenges that complicate the relevant techniques and the interpretation of the results have not yet been fully explored. This article investigates some of these issues, with a focus on optimizing the technical approach and quantifying the key systematics. Section 2 designs models of the physical conditions and kinematics expected in disks to serve as ‘controls’ that frame our inquiries. Section 3 outlines the adopted approach for converting those physical models into realistic simulated datasets. Section 4 describes how to extract the disk velocity field and infer M_d , and Section 5 explores the systematics (accuracy) and precision. Section 6 demon-

strates the approach on an archival ALMA dataset and outlines the prospects for deploying what we learned, along with some complications not yet considered in detail. Section 7 summarizes the key conclusions.

2. DISK MODELS

The primary goal of this article is to explore the precision and systematic uncertainties of dynamical M_d measurements. To that end, we designed synthetic datasets where the *true* (input) properties of the disks are known, and then investigated how well we could recover those inputs under various conditions. This section introduces a parametric disk model. The adopted prescription approximates more sophisticated modeling treatments, but promotes more intuition for factors that complicate dynamical measurements of M_d . The physical conditions, kinematics, and molecular abundances are described in Sections 2.1, 2.2, and 2.3, respectively. A set of fiducial models are assigned in Section 2.4, and used to illustrate some key links between structure and dynamics.

2.1. Physical Conditions

We defined model structures in cylindrical polar coordinates (r, ϕ, z) , assuming axisymmetry (no dependence on azimuth ϕ) and mirror symmetry about the midplane ($z = 0$). The gas density distribution ρ is defined to be in vertical hydrostatic equilibrium,

$$\frac{\partial P}{\partial z} = -\rho g_z, \quad (1)$$

where P is the pressure and g_z is the vertical component of the gravitational acceleration. Assuming an ideal gas with $P = \rho c_s^2$, Eq. (1) can be written as

$$-\frac{1}{\rho} \frac{\partial \rho}{\partial z} = \frac{g_z}{c_s^2} + \frac{2}{c_s} \frac{\partial c_s}{\partial z}, \quad (2)$$

where c_s is the sound speed,

$$c_s = \sqrt{\frac{k_B T}{\mu m_H}}, \quad (3)$$

with T the temperature, k_B the Boltzmann constant, μ ($= 2.37$) the mean molecular weight, and m_H the mass of a H atom. The vertical acceleration was decomposed into stellar and disk contributions, $g_z = g_{z,*} + g_{z,d}$. The stellar term is the vertical derivative of the potential Φ_* ,

$$g_{z,*} = \frac{\partial \Phi_*}{\partial z} = \frac{GM_* z}{(r^2 + z^2)^{3/2}}, \quad (4)$$

where G is the gravitational constant. The disk term is

$$g_{z,d} = 2\pi G\Sigma, \quad (5)$$

a simplification for a mass distribution that is vertically thin and radially infinite (Armitage 2010). While neither of those assumptions is technically correct, this still

serves as a reasonable approximation for our purposes. Density structures $\rho(r, z)$ were determined by numerical integration of Eq. (2) for a given M_* , temperature structure $T(r, z)$, and surface density profile $\Sigma(r)$.

The temperatures are bounded by the midplane (T_{mid}) and atmosphere (T_{atm}) profiles, using a simplification of the behavior adopted by [Dullemond et al. \(2020\)](#),

$$T = T_{\text{mid}} + f_T(r, z) (T_{\text{atm}} - T_{\text{mid}}), \quad (6)$$

where

$$f_T(r, z) = \frac{1}{2} \tanh \left[\frac{(z/r) - a_z}{w_z a_z} \right] + \frac{1}{2}. \quad (7)$$

The location (midpoint) of the vertical thermal transition is set by a_z , and its width is controlled by w_z . The radial temperature profiles

$$T_{\text{mid}} = T_{\text{m},0} \left(\frac{r}{r_0} \right)^{-q}; \quad T_{\text{atm}} = T_{\text{a},0} \left(\frac{r}{r_0} \right)^{-q} \quad (8)$$

define the radial thermal structure.

The surface density profile was defined as an exponentially tapered power-law,

$$\Sigma = \Sigma_0 \left(\frac{r}{r_0} \right)^{-p} \exp \left[- \left(\frac{r}{r_t} \right)^\gamma \right]. \quad (9)$$

This prescription is flexible enough to cover the common assumptions in the literature: for example, $\gamma = 2 - p$ reproduces the [Lynden-Bell & Pringle \(1974\)](#) viscous disk similarity solution, and $\gamma = \infty$ is equivalent to the sharp radial truncation of a power-law at r_t . All parametric normalizations were defined at $r_0 = 10$ au.

2.2. Kinematics

The bulk motions of the disk models were assumed to be solely in the azimuthal direction, with three contributors to the net velocity distribution,

$$v_\phi^2 = r \underbrace{\frac{\partial \Phi_*}{\partial r}}_{v_*^2} + \underbrace{\frac{r}{\rho} \frac{\partial P}{\partial r}}_{\varepsilon_p} + r \underbrace{\frac{\partial \Phi_d}{\partial r}}_{\varepsilon_g}. \quad (10)$$

The first term in Eq. (10) accounts for the orbital motion in the stellar potential (Φ_*), defined as

$$v_*^2 = \frac{GM_* r^2}{(r^2 + z^2)^{3/2}} = v_K^2 \frac{r^3}{(r^2 + z^2)^{3/2}}, \quad (11)$$

where

$$v_K = \sqrt{\frac{GM_*}{r}} = r \Omega_K \quad (12)$$

is the Keplerian velocity and Ω_K is the Keplerian angular velocity. Note that $v_* = v_K$ at the midplane ($z = 0$).

The second term (ε_p) accounts for radial pressure support, and the third term (ε_g) accounts for the disk self-gravity (Φ_d denotes the disk potential): ε_p can take positive or negative values, but ε_g is always positive because the gravitational field ($\partial \Phi_d / \partial r$) is an increasing function of r . The stellar potential (v_*) dominates the velocity field over most of the disk, with the additional two terms present as small deviations. However, for the diffuse gas reservoir in tapered models (finite γ) at $r > r_t$, the Σ taper implies that ε_p can control the dynamics.

The deviations ε_p and ε_g were calculated numerically, with ε_g computed following the [Bertin & Lodato \(1999\)](#) approximation for the field,

$$\frac{\partial \Phi_d}{\partial r} = \frac{G}{r} \int_0^\infty \xi(k) \sqrt{\frac{r'}{r}} k \Sigma(r') dr', \quad (13)$$

with

$$\xi(k) = \mathcal{K}(k) - \frac{1}{4} \left(\frac{k^2}{1 - k^2} \right) \left[\frac{r'}{r} - \frac{r}{r'} + \frac{z^2}{rr'} \right] \mathcal{E}(k), \quad (14)$$

where \mathcal{K} and \mathcal{E} are complete elliptic integrals of the first and second kind, and k is a composite coordinate

$$k = \left[\frac{4r r'}{(r + r')^2 + z^2} \right]^{1/2}. \quad (15)$$

For pedagogical purposes, we defined *residual* velocity fields that focus on the contributions of pressure support and self-gravity individually and in combination,

$$\begin{aligned} \Delta v_p &= \sqrt{v_*^2 + \varepsilon_p} - v_* \\ \Delta v_g &= \sqrt{v_*^2 + \varepsilon_g} - v_* \\ \Delta v_\phi &= v_\phi - v_*, \end{aligned} \quad (16)$$

that will help serve as visualization aids (e.g., see [Rosenfeld et al. 2013](#), their Figure 10).

2.3. Molecular Abundances

As noted in Section 1, the abundance distribution for the molecule of interest is a crucial factor in converting physical conditions into line emission. The focus here is CO. Motivated by astrochemical models ([Aikawa et al. 1996, 2002](#)), we set a constant abundance X_{CO} in a vertical layer (cf., [Qi et al. 2008](#)). The lower boundary of that layer is defined as the isotherm where CO adsorbs onto dust grains: $T = T_{\text{frz}}$ ([van Zadelhoff et al. 2001](#)). The upper boundary is the surface $z_{\text{crit}}(r)$ associated with a critical column density σ_{crit} ,

$$\sigma_{\text{crit}} = \int_0^{z_{\text{crit}}} \rho dz, \quad (17)$$

meant to emulate the photodissociation threshold ([van Zadelhoff et al. 2003; Aikawa & Nomura 2006](#)).

Table 1. Fiducial Model Parameters: fixed $M_d = 0.1 M_\odot$ and $d = 150$ pc

	Σ_0	r_t	p	γ	$T_{m,0}$	$T_{a,0}$	q	a_z	w_z	M_*	T_{frz}	σ_{crit}	X_{CO}	Δx	Δy	i	ϑ	v_{sys}
	(g/cm^2)	(au)			(K)	(K)				(M_\odot)	(K)	(g/cm^2)		($''$)	($''$)	($^\circ$)	($^\circ$)	(m/s)
model A	189	75	1	1	40	120	0.5	0.1	0.2	1.0	20	0.01	10^{-5}	0	0	30	130	0
model B	100	160	1	2	40	120	0.5	0.1	0.2	1.0	20	0.01	10^{-5}	0	0	30	130	0
model C	68	230	1	4	40	120	0.5	0.1	0.2	1.0	20	0.01	10^{-5}	0	0	30	130	0

NOTE—The reference radius was set to $r_0 = 10$ au.

We defined the abundance structure as

$$\rho_{\text{CO}} = D_{\text{CO}} X_{\text{CO}} \rho, \quad (18)$$

where the depletion factor for regions outside the abundant layer is a step-function

$$D_{\text{CO}} = \begin{cases} 1 & \text{if } T \geq T_{\text{frz}} \text{ and } z \leq z_{\text{crit}}, \\ 0.001 & \text{otherwise.} \end{cases} \quad (19)$$

We adopted $X_{\text{CO}} = 10^{-5}$ in these models, roughly the mean value measured by Zhang et al. (2021) and predicted in detailed evolution models by Krijt et al. (2020).

2.4. Fiducial Models

We designed three fiducial disk models to guide an exploration of the quality of M_d inferences, with the parameters compiled in Table 1. These models all consider a $M_* = 1 M_\odot$ star hosting a $M_d = 0.1 M_\odot$ disk, but with different $\Sigma(r)$ behaviors at large r that permit us to focus on variations associated with regions where the dynamical signal of self-gravity is strongest.

Figure 1 shows radial profiles of Σ , encircled mass

$$M_d(< r) = \int_0^r \Sigma 2\pi r' dr', \quad (20)$$

and the Toomre (1964) instability parameter

$$Q = \frac{c_s \Omega_K}{\pi G \Sigma} \quad (21)$$

for each model. These models are formally gravitationally stable ($Q > 1$), with minimum Q values ≈ 3 . The key variation between models is in the Σ taper (γ): p was fixed, r_t was adjusted to force the models to have the same effective emission size (Section 3).

The thermal structures for the fiducial models are identical: Figure 2 shows their $T(r, z)$ distribution. The associated parameters were chosen to emulate the predictions from more sophisticated radiative transfer models, particularly for scenarios where modest dust settling (less turbulent stirring) introduces a steeper vertical temperature gradient at lower altitudes (e.g., D’Alessio et al. 2006). Figure 3 shows the volume density distributions for each model (where $n = \rho/\mu m_{\text{H}}$) and marks the

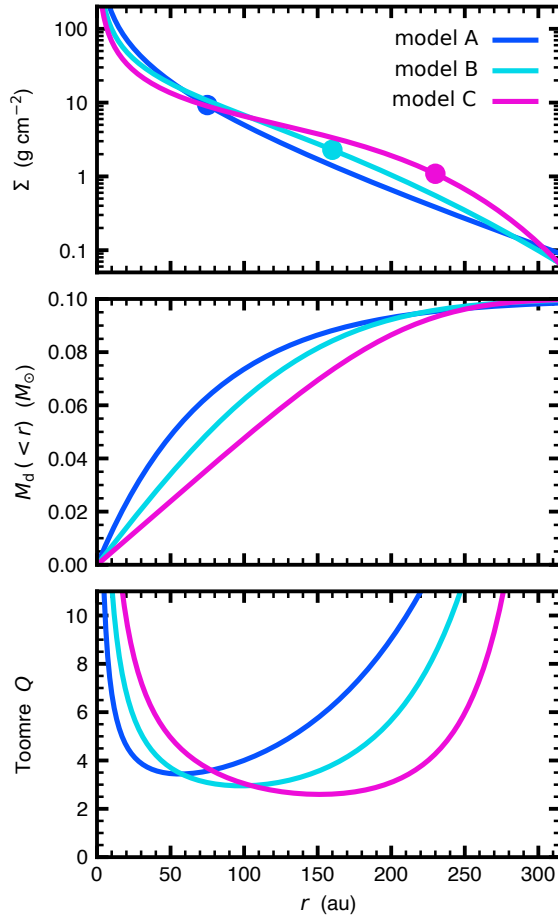


Figure 1. The surface density (circles mark r_t), encircled mass, and Toomre stability parameter radial profiles for the fiducial models. Note that these models are formally stable, even though the canonical mass ratio ($M_d/M_* = 0.1$) is high.

layer where CO is abundant in the gas-phase, bounded between the T_{frz} isotherm and z_{crit} surface. These layers span $z/r \approx 0.1$ – 0.3 outside the midplane CO snowline ($r = 40$ au), consistent with ALMA measurements (Law et al. 2021a, 2022; Rich et al. 2021; Izquierdo et al. 2021; Paneque-Carreño et al. 2023). Note that the “pinch” in the $n(r, z)$ distribution near $z/r = 0.1$ is a consequence of the steep transition in the adopted $T(z)$ prescription.

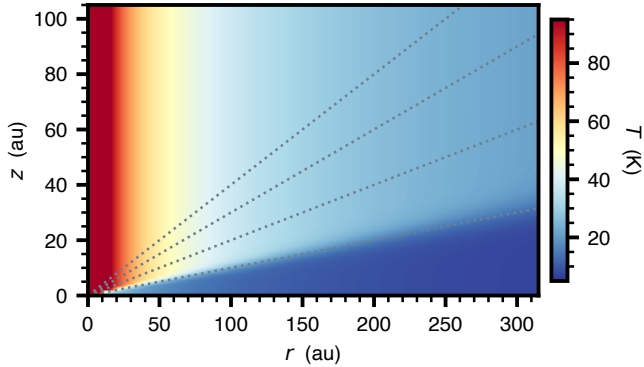


Figure 2. The temperature structure for the fiducial models. Dotted curves mark $z/r = 0.1, 0.2, 0.3,$ and 0.4 .

Figure 4 highlights the residual velocity fields (Eq. 16). The Δv_p contributions exhibit a vertically layered structure, where deviations near the base of the CO-rich layer are slightly ($|\Delta v_p|/v_* \sim 1\%$, or $|\Delta v_p| \approx 10\text{--}30 \text{ m s}^{-1}$) negative before diverging to much stronger negative deviations for $r \gg r_t$ (in the Σ taper, where ε_p dominates). The flared density distribution reverses the sign of the radial pressure gradient at higher altitudes, transitioning to positive Δv_p residuals for $z/r \gtrsim 0.25$ (or higher in the Σ taper). In contrast, Δv_g increases with r until Σ tapers (where the disk potential gradient diminishes) and is always positive. The largest Δv_g are at the mid-plane, but the vertical variation is modest.

Assuming that the top of the CO-rich layer coincides with the spectral line “photosphere” (see Sect. 5.1), Figure 5 summarizes the key behaviors of the observable residual velocities. We see the kinematic deviations from pressure support dominate at both small and large r : self-gravity is a modest contributor when a small fraction of the disk mass is encircled, and the pressure gradient becomes very strong well out in the Σ taper. The contributions of pressure support and self-gravity are comparable ($\Delta v_p \sim \Delta v_g$) at radii within a factor of \sim two around r_t . The transition between these regimes is determined by the Σ gradient (γ) in the taper (which motivated the fiducial parameter choices).

3. SIMULATED DATA

ALMA observations of molecular emission lines can be powerful probes of disk dynamics (Pinte et al. 2023). The motions of interest here are small perturbations on the “background” field, with $|\Delta v_\phi|/v_* \lesssim 5\%$. The precision at which such subtle features are measured depends critically on the sensitivity in the selected tracer (e.g., Teague et al. 2022), so observers have focused on bright, optically thick line emission from abundant species. The discussion here is focused on the $J=2-1$ pure rotational transition of CO, though we also address some benefits of extending this analysis to other transitions, isotopologues, and species. This section describes how we translated the physical and dynamical conditions of the

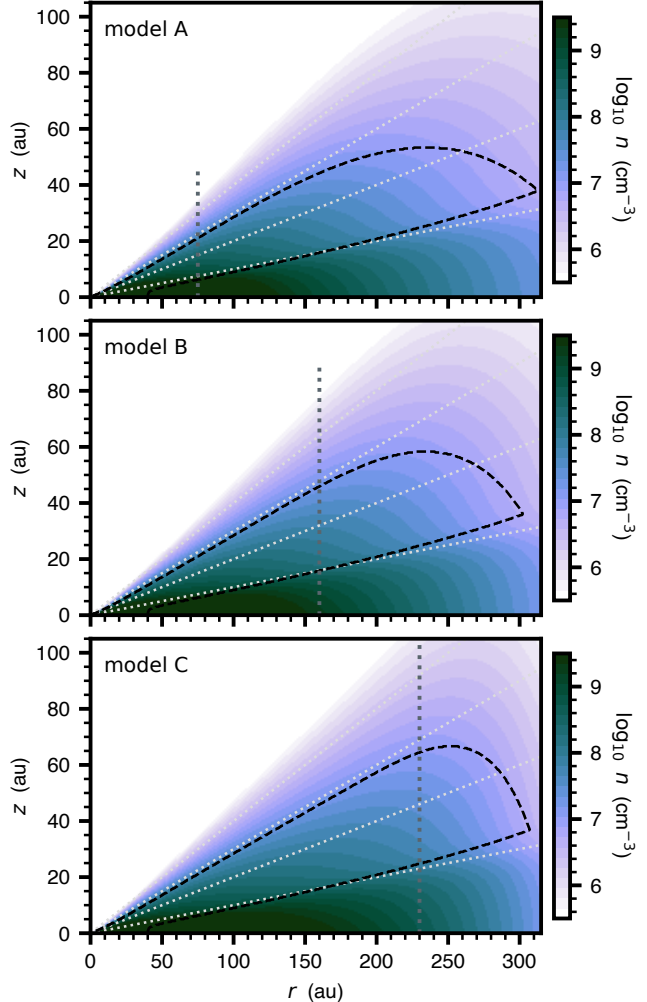


Figure 3. The (volume) density structures (on a \log_{10} scale) for the fiducial models. The dashed contour regions enclose the CO-rich layer, and the dotted vertical lines mark r_t . Other annotations are as in Figure 2.

fiducial models into (synthetic) observations (Sect. 3.1), and explains how the kinematic perturbations of interest are manifested in such datasets (Sect. 3.2).

3.1. Model Processing to Simulated Datasets

Using the prescription we described above and the parameters in Table 1, we relied on the (local thermodynamic equilibrium) excitation and raytracing capabilities of RADMC-3D (Dullemond et al. 2012) to compute synthetic spectral line cubes. The model properties were assigned on a fixed grid in spherical coordinates (some nuances of that procedure are detailed in Appendix A). The CO quantum properties were compiled from the LAMDA database (Schöier et al. 2005). Line profiles were assumed to be Gaussian with widths set solely by thermal broadening (see Flaherty et al. 2018).

Some additional extrinsic quantities are used in the raytracing (see Table 1). The observing geometry is de-

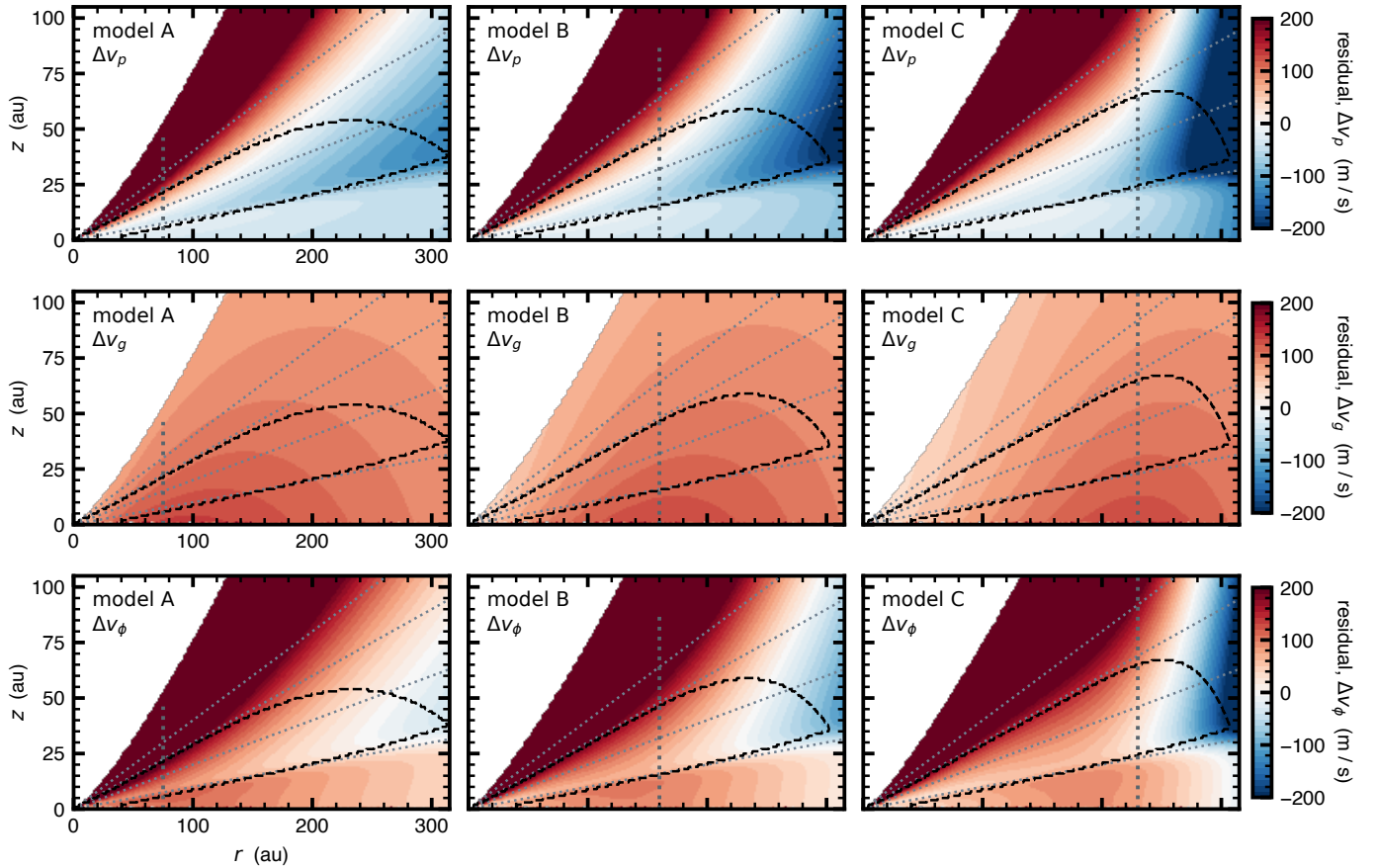


Figure 4. The residual velocity structures (Eq. 16) for the fiducial models (linear scale). The annotations are as in Figure 3.

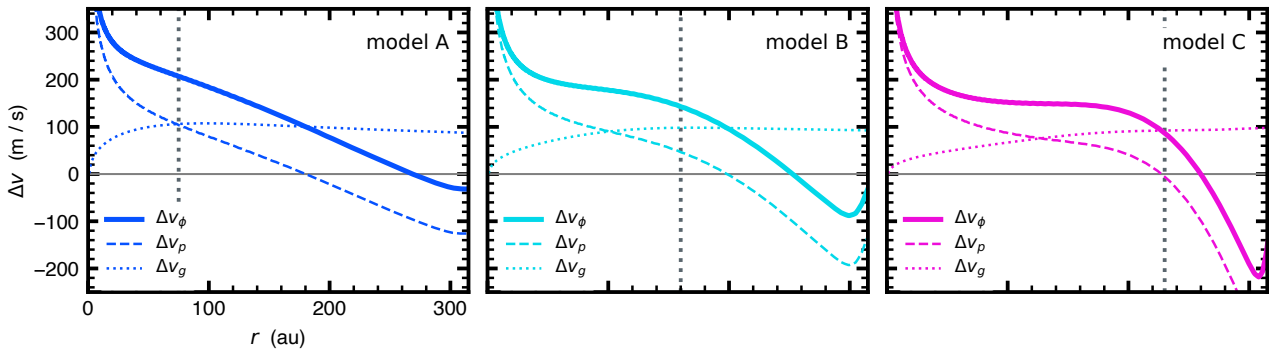


Figure 5. Decompositions of the velocity residuals (Eq. 16) for each model along the top boundary of the CO-rich layer (see Fig. 4), which coincides with the CO emission surface (see Sect. 5.1). The vertical lines mark r_t as a point of reference.

terminated by the distance d and the sky-projected inclination i and position angle ϑ . We assigned $d = 150$ pc, $i = 30^\circ$, and $\vartheta = 130^\circ$, using the convention where ϑ is the angle E of N to the redshifted side of the major axis, and set the systemic velocity v_{sys} and disk center $(\Delta x, \Delta y)$ to the origins of their respective reference frames (formally, $\Delta x = \Delta\alpha \cos\delta$ and $\Delta y = \Delta\delta$, where $\{\Delta\alpha, \Delta\delta\}$ are the R.A. and Declination offsets from the observed pointing). The RADMC-3D raytracing was con-

figured to produce a model cube on specified spatial and spectral grids. We adopted 10 milliarcsecond pixels in a 1024×1024 ($\sim 10''$) field of view and channels with a native spacing of 30.5 kHz (~ 40 m s $^{-1}$ at the $J=2-1$ rest frequency) that span ± 6.5 km s $^{-1}$ around v_{sys} .

We designed a template for ALMA observations of the CO $J=2-1$ line (rest frequency 230.538 GHz) that emulates the kind of program we expect to be most fruitful for dynamical M_d measurements. It comprises a group

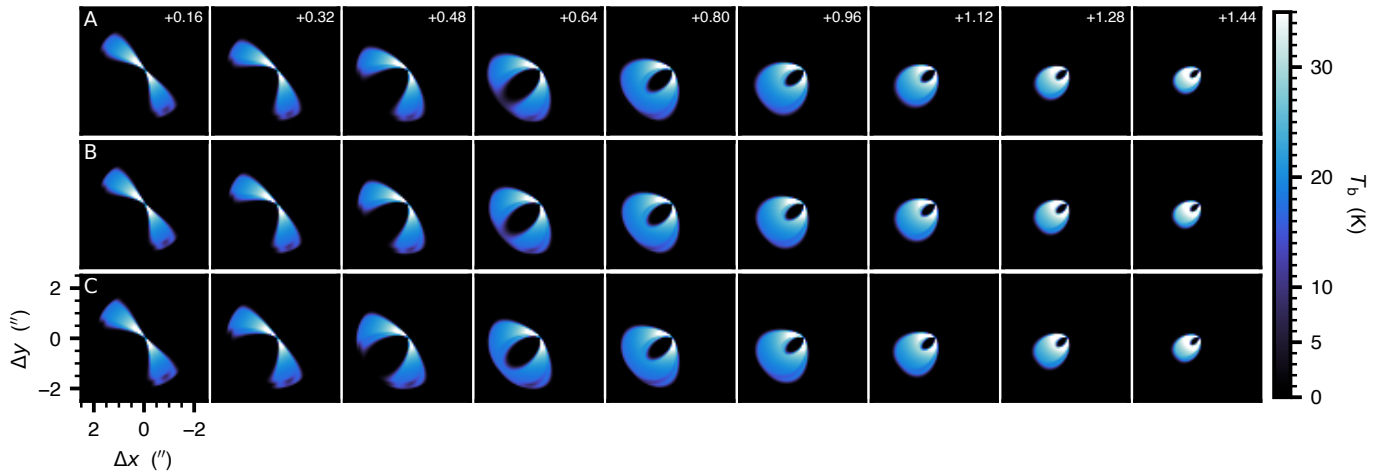


Figure 6. A representative subset of the *raw* channel maps for the fiducial models (see Table 1), on the same (Rayleigh-Jeans) brightness temperature scale. This shows a portion of the redshifted side of the line, with the LSRK velocities (in km s^{-1}) noted in the top right corners of the panels in the top row. These maps are showing only every other 80 m s^{-1} channel, to illustrate the behavior over a broader projected velocity range. Each panel corresponds to a 750 au field of view.

of five 1 hour execution blocks (EBs): one with the C-4 configuration (15–780 m baselines), and four with the C-7 configuration (64–3600 m baselines). We assumed these occur during Cycle 11, with observations in C-4 on 2025 March 1 ($\text{HA} = \pm 0.5^{\text{h}}$), and C-7 on 2025 May 20 and 25 (both with consecutive EBs at HA ranges from -1 to 0^{h} and 0 to 1^{h}). For each EB, we generated a set of Fourier (u, v) coordinates for each (pre-averaged) 18 s timestamp, with an associated grid of native channels in the kinematic local standard of rest (LSRK) frame appropriate for the time, date, and source location (R.A. = 16^{h} , Decl. = -30°) for a topocentric grid that was fixed at the initial timestamp.

A model cube was created at the LSRK frequencies corresponding to the topocentric channels at the midpoint of each EB. Their Fourier transforms were sampled onto the template (u, v) spatial frequencies using the `vis_sample` package (Loomis et al. 2018). The visibility spectra were interpolated to the appropriate LSRK frequencies at each timestamp. These *pure* visibility spectra were converted into two datasets. For one, we convolved the pure spectra with the default ALMA spectral response function (the Fourier transform of the Hann window function). For the other, we injected noise into the pure spectra using random draws from a Gaussian distribution with mean 0 and standard deviation scaled to produce the RMS expected ($2.3 \text{ mJy beam}^{-1}$ per 80 m s^{-1} channel) for the integration time (based on the online ALMA exposure time calculator¹), and then convolved with the spectral response function. Finally, the datasets for all EBs were concatenated. The simula-

tions and post-processing steps were computed with the `csalt` package (Andrews et al., *in preparation*).

These two datasets were then converted into their respective ‘observed’ cubes with the standard imaging process using the `CASA/tclean` task (CASA Team et al. 2022; Cornwell 2008). We set $0''.02$ pixels and a channel spacing of 80 m s^{-1} (matching the spectral resolution) spanning $v_{\text{sys}} \pm 5.6 \text{ km s}^{-1}$, and used Briggs weighting with `robust = +1` and `multiscale` parameters that included point source and Gaussian scales at 10, 30, and 50 pixel FWHMs. These cubes were `cleaned` to a threshold of $4.6 \text{ mJy beam}^{-1}$ (or 7.4 K , twice the noise level) using a Keplerian mask (Teague 2020) that was convolved with a $\text{FWHM} = 0''.15$ Gaussian. They have synthesized beams with $\text{FWHM} = 0''.13 \times 0''.11$ (at P.A. = 95°).

Three versions of a cube are produced for each model. The *sampled* cube treats the spatial and spectral sampling of ALMA observations, in the absence of noise. The *noisy* cube is the version of the sampled cube with realistic noise. And the *raw* cube was computed as the direct output of RADMC-3D raytracing on these *imaged* velocity channels at the full ($0''.01$) resolution. The raw cube is intended as a reference for probing the effects of line radiative transfer on inferred disk properties without observational sampling issues or noise.

Figure 6 highlights a representative subset of channel maps from the raw cubes for the fiducial models, to illustrate their general behavior and subtle differences. Figure 7 compares the three different types of cubes – raw, sampled, and noisy – using model B as an example.

3.2. Dynamical Effects on the Cubes

While the fiducial models were tuned to provide some insight on how $\Sigma(r)$ influences measurements of the disk dynamics, their parameters were selected to ensure that

¹ <https://almascience.nrao.edu/proposing/sensitivity-calculator>

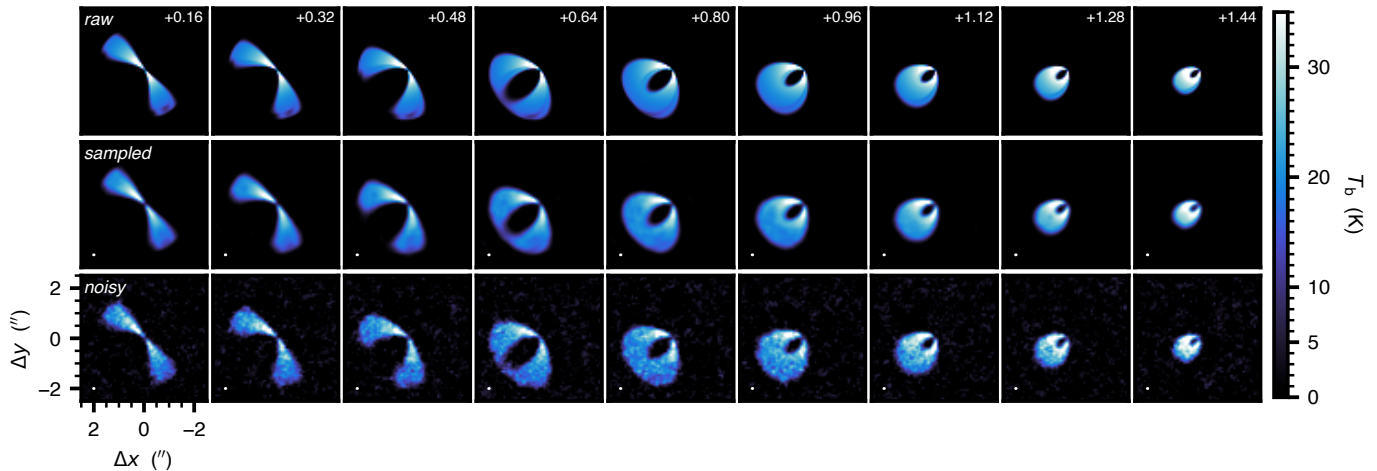


Figure 7. The same subset of channel maps (and annotations, colorscale) as in Figure 6 for model B, now showing (from top to bottom rows) the *raw*, *sampled*, and *noisy* versions of the cube (note the top row here is identical to the second row in Figure 6). The FWHM synthesized beam dimensions are shown as (small) white ellipses in the bottom left corners of the sampled and noisy channel maps (the effective pixel resolution in the raw channel maps is $\sim 10\times$ smaller).

the resulting cubes are similar enough that data quality is not a critical factor in those efforts. These models have the same CO fluxes (7 Jy km s^{-1}) and sizes (280 au; defined as the radius that encircles 90% of the flux), designed to match typical disks with $M_* \approx 1 M_\odot$ host stars (Sanchis et al. 2021; Long et al. 2022).

The kinematic deviations from pressure support and self-gravity impart subtle, complex changes in the emission distribution. In Figure 8, these effects are decomposed for variants of raw model B channel maps (made from distinct RADMC-3D calculations), using the same parameters but different contributions to the net velocity field. The top row is the reference: it includes only the stellar potential ($v = v_*$). The next two rows show the residuals with respect to that reference for models with the individual effects of pressure support ($v = v_* + \Delta v_p$) or self-gravity ($v = v_* + \Delta v_g$), respectively. And the bottom row shows the residuals for a model with the composite velocity field ($v = v_\phi$, defined in Eq. 10).

To interpret Figure 8, it helps to revisit the decompositions of the residual velocity profiles in Figure 5. The $\Delta v_p(r)$ for model B decreases and changes sign beyond r_t (~ 200 au). This slowed rotation manifests as enhanced emission at larger radii near v_{sys} , with the opposite behavior at smaller radii in the line wings. The increasing $\Delta v_g(r)$ shifts the emission morphology to slightly faster rotation at all r ; however, the gradient in Δv_g generates more complex behavior than a v_* -only model with enhanced M_* , in part due to radiative transfer effects in the line wings. The combination of these effects imparts complicated deviations for the composite field.

Figure 9 illustrates how these same behaviors appear in a spatially-integrated sense, with spectra that demonstrate how the kinematic contributions shift around flux in v_{obs} . Comparing the $v = v_* + \Delta v_p$ and $v = v_\phi$ cases in

Figures 8 and 9 offers some indication of the spectral impact of varying M_d/M_* , from negligible ($\ll 1\%$) to substantial (10%) values. The effects are subtle, but they are also accessible for data with sufficient resolution and sensitivity. The next sections describe approaches for extracting such information from the data and using it to measure those quantities of interest (i.e., M_d).

4. KINEMATICS ANALYSIS: CONCEPTS

The most principled approach to measuring M_d would integrate the steps described in Sections 2 and 3 into a forward-modeling framework, deploying a parametric structure and radiative transfer calculations to self-consistently infer posterior distributions for the full suite of input parameters conditioned on the visibility spectra. But that is an expensive task, since each likelihood computation is slow and the high dimensionality (there are 18 parameters in the “simple” prescription here) of the problem requires an expansive exploration of posterior-space to quantify the globally optimized parameters.

Fortunately, we only care here about the velocity field (though see Section 4.3), and will focus on high-quality data with appropriate spatial and spectral resolution for the task. So instead, we further developed a simplified approach (Veronesi et al. 2021; Lodato et al. 2023; Martire et al. 2024) that forward-models a distilled measurement of $v_\phi(r)$ to constrain Σ (and M_d). This framework assumes the disk structure and kinematics are axisymmetric, and that no external contributions (e.g., cloud or envelope contamination) are present. This section explains the process for extracting and modeling the disk kinematics. The procedure is hierarchical, with four sequentially linked ‘layers’ of data extraction and inference that are each outlined in more detail below. Figure 10 provides a visual summary of the procedure as a guide.

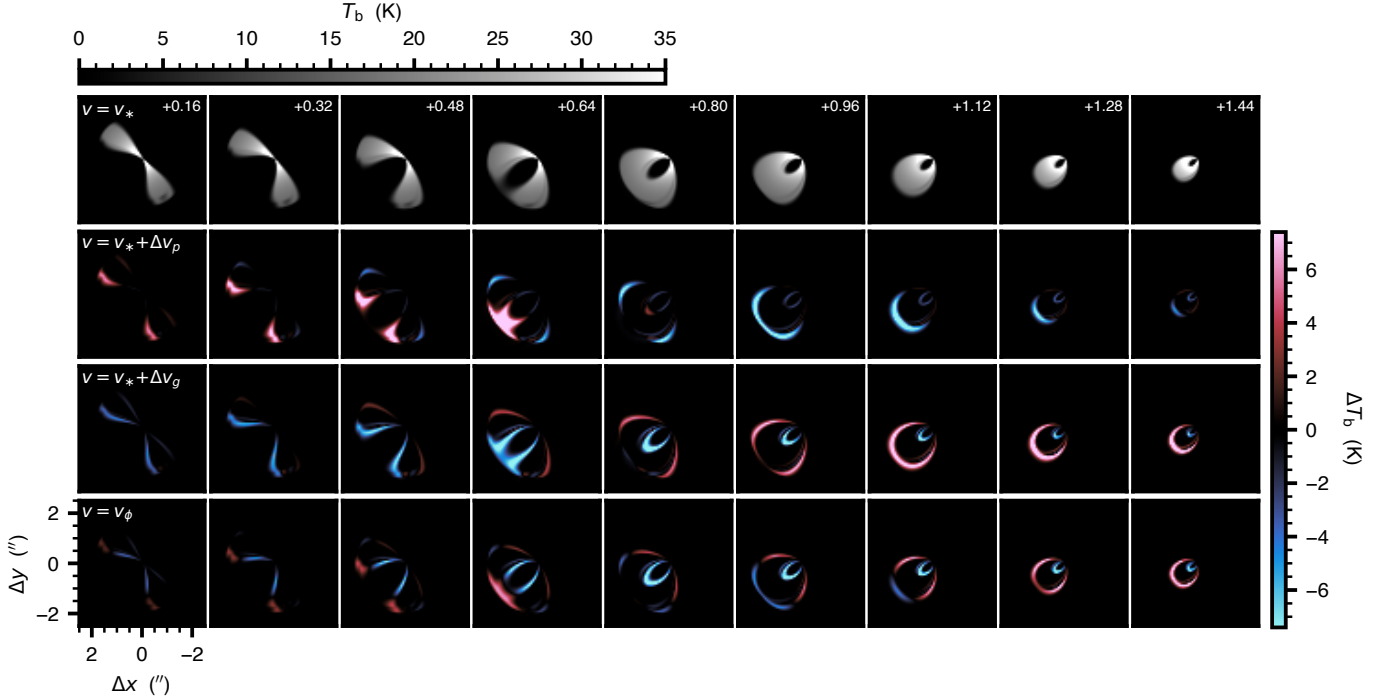


Figure 8. The top row shows a set of *raw* channel maps for a variant of model B where the velocity field is determined solely by the stellar potential: $v = v_*$ (Eq. 11). The subsequent rows show residual maps, constructed as the differences between channel maps for other variants of the velocity field and the top row. From top to bottom, these are for velocity field contributions that include the stellar potential plus pressure support ($v = v_* + \Delta v_p$, see Eq. 16; no self-gravity), the stellar potential plus self-gravity ($v = v_* + \Delta v_g$, see Eq. 16; no pressure support), and the stellar potential plus both pressure support and self-gravity ($v = v_\phi$, see Eq. 10; the fiducial model B case). The annotations are as in Figure 6.

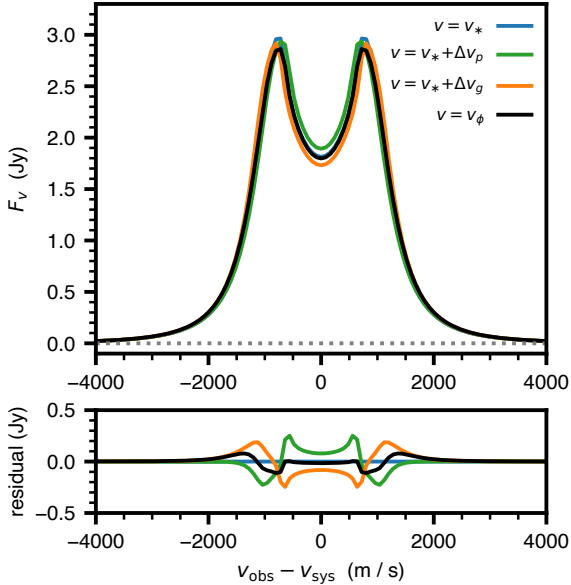


Figure 9. (*top*) The spatially integrated spectra for model B variants with different contributions to the velocity field (integrated from the raw cubes used to make Fig. 8). (*bottom*) The differences with respect to the v_* -only model (blue).

4.1. Layer 1: Geometry

The geometric conversions between the observed (sky-projected) and disk spatial and spectral reference frames are critical for analyzing the spectral line emission. The relevant coordinate transformations are specified by the spatial projection angles (i and ϑ), spatial translations (Δx and Δy), and systemic velocity (v_{sys}) in the LSRK frame. The **Layer 1** task is to measure these parameters in terms of samples of the posterior probability distribution, $p(\theta_1 | \text{data})$, where we have grouped the parameters in shorthand as $\theta_1 = [i, \vartheta, \Delta x, \Delta y, v_{\text{sys}}]$ and *data* refers to some (here unspecified) set of measurements.

The mechanics are left deliberately vague here, since in practice we decided to draw from *presumed* distributions in this layer (Sect. 5). Often, the spatial parameters in θ_1 are estimated from the mm continuum (Huang et al. 2018b), infrared scattered light (de Boer et al. 2016), or spectral line data (Teague et al. 2021). A precise v_{sys} can be found from a straightforward measurement exploiting symmetry in the channel maps.

4.2. Layer 2: Emission Surface

The **Layer 2** task is to locate where the emission originates. The radial distribution of the heights (z) that represent the spectral line *photosphere* depends on the excitation conditions and optical depths along each line-

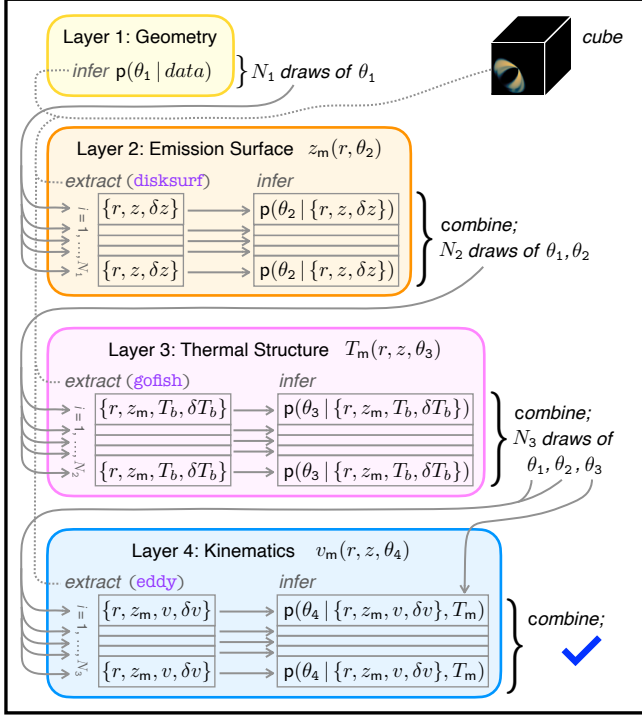


Figure 10. A flowchart of the layered analysis procedure to quantitatively interpret disk kinematics.

of-sight from the observer (note the implicit conditioning on θ_1). Locating this emission surface requires an extraction step, where a set of surface “coordinates” $\{r, z, \delta z\}$ (with δz representing uncertainties) are distilled from a cube, and an inference step, where those coordinates are fit with a surface model, $z_m(r)$.

The surface coordinates were determined by locating intensity peaks in isovelocity “loops” in channel maps deprojected into the disk-frame (Pinte et al. 2018), using the `disksurf` package (Teague et al. 2021). The δz were assigned to be the ratio of the beam FWHM and pixel SNR. Coordinate extractions were limited to $160 \leq |v_{\text{obs}} - v_{\text{sys}}| \leq 1680 \text{ m s}^{-1}$: further into the wings the emission is too compact, and near v_{sys} the deprojection is ambiguous. An initial extraction clipped pixels outside the range $0 \leq z/r \leq 1$ and where $T_b \leq 3.7 \text{ K}$ (`min_zr=0, max_zr=1, min_SNR=1`). Two additional iterations were performed, using the initial surfaces to define kinematic masks that were convolved with Gaussian kernels having FWHM of 2 and 1 beams (`nbeams=[2, 1]`) for clips at $T_b = 7.4$ and 11.1 K (`min_SNR=[2, 3]`): pixels corresponding to $z/r < 0.05$ were excluded.

A resulting set of $\{r, z, \delta z\}$ was used to infer the parameters of a surface model (Law et al. 2020),

$$z_m(r, \theta_2) = z_0 \left(\frac{r}{150 \text{ au}} \right)^\varphi \exp \left[- \left(\frac{r}{r_z} \right)^\psi \right], \quad (22)$$

using $\theta_2 = [z_0, \varphi, r_z, \psi, f_{\text{surf}}]$ as shorthand notation for the surface parameters. We defined a log-likelihood

function $\ln \mathcal{L}_2 = \ln p(\{r, z, \delta z\} | \theta_2)$ as

$$\ln \mathcal{L}_2 = -\frac{1}{2} \sum_i \left[\frac{(z_i - z_m(r_i))^2}{s_i^2} + \ln 2\pi s_i^2 \right], \quad (23)$$

$$\text{with } s_i^2 = \delta z_i^2 + f_{\text{surf}}^2 z_m(r_i)^2.$$

The nuisance parameter f_{surf} is designed to account for under-estimated scatter in z . There is an implicit conditioning on θ_1 in \mathcal{L}_2 , related to the $\{r, z, \delta z\}$ extraction.

To propagate the **Layer 1** information into the emission surfaces, we drew N_1 random θ_1 from the posterior samples and extracted the corresponding set of surface coordinates $\{r, z, \delta z\}$ for each. Then we sampled the (log-)posterior distribution for each draw,

$$\ln p(\theta_2 | \{r, z, \delta z\}) \propto \ln \mathcal{L}_2 + \ln p(\theta_2), \quad (24)$$

where $p(\theta_2)$ is the prior, using the `emcee` Monte Carlo Markov Chain sampler (Foreman-Mackey et al. 2013; see Sect. 5). The resulting N_1 sets of posterior samples were combined. That *über-set* of posterior samples is too large to propagate. Instead, we drew a representative subset of N_2 values $\{\theta_1, \theta_2\}$ from it to use in the next layer.

4.3. Layer 3: Thermal Structure

The aim of **Layer 3** is to provide some constraints on the disk temperature structure, and thereby the vertical density distribution and associated kinematic contributions. The idea is to assume the line emission is optically thick and thermalized. In that case, the radial intensity profile is a proxy for the gas temperature profile along the emission surface. With a judicious selection of priors, this offers some (limited) constraint on $T(r, z)$.

The extraction step in this layer starts with computing the peak intensity (moment-8) map from the cube with the `bettermoments` package (Teague & Foreman-Mackey 2018; Teague 2019). Next, the `gofish` package (Teague 2019a) was used on that peak intensity map to extract an azimuthally-averaged brightness temperature (using the full Planck function, not the Rayleigh-Jeans limit) profile along the emission surface – a set of $\{r, z_m, T_b, \delta T_b\}$ – for each $\{\theta_1, \theta_2\}$ draw from **Layer 2**.

For the inference step, we interpreted those brightness temperature profiles with the model

$$T_m(r, z, \theta_3) = T(r, z_m), \quad (25)$$

as defined in Eq. (6)–(8), with $\theta_3 = [T_{m,0}, T_{a,0}, q, a_z, w_z, f_{\text{temp}}]$. For a single line, this is an under-constrained parameter-space. Nevertheless, this setup is useful to maintain in the hierarchy: it allows us to meaningfully propagate that ambiguity into the inference in the final layer, even if based largely on the priors. Moreover, in cases where observations of multiple lines are available that probe a range of emission surface heights, it can naturally incorporate that added information into improved constraints on the thermal structure.

The inference procedure is the same as for **Layer 2**. We defined a Gaussian (log-)likelihood function $\ln \mathcal{L}_3 = \ln \mathbf{p}(\{r, z_m, T_b, \delta T_b\} | \theta_3)$ as

$$\ln \mathcal{L}_3 = -\frac{1}{2} \sum_i \left[\frac{(T_b(r_i) - T_m(r_i, z_m))^2}{s_i^2} + \ln 2\pi s_i^2 \right],$$

$$\text{with } s_i^2 = \delta T_b(r_i)^2 + f_{\text{temp}}^2 T_m(r_i, z_m)^2. \quad (26)$$

where f_{temp} is a nuisance parameter designed to account for any under-estimated scatter. Again, there is implicit conditioning on θ_1 and θ_2 in the data (T_b profile) extraction. For each $\{\theta_1, \theta_2\}$ draw and associated $\{r, z_m, T_b, \delta T_b\}$, the (log-)posterior distribution

$$\ln \mathbf{p}(\theta_3 | \{r, z_m, T_b, \delta T_b\}) \propto \ln \mathcal{L}_3 + \ln \mathbf{p}(\theta_3) \quad (27)$$

was sampled as before; the N_2 sets of posterior samples were combined and a representative subset of N_3 values $\{\theta_1, \theta_2, \theta_3\}$ were then drawn to proceed.

4.4. Layer 4: Kinematics

This final layer follows the theme set in the previous ones, with an extraction and inference that is now focused on the kinematics. The parameters of interest in **Layer 4** describe the contributions of the stellar and disk potentials to the gas motions – M_* and the prescription for $\Sigma(r)$ (and thereby M_d), respectively.

For each draw of $\{\theta_1, \theta_2\}$ from **Layer 3** (θ_3 does not factor in yet), we extracted a velocity profile along the emission surface using the `eddy` package (Teague 2019b). The pixel coordinates in the cube were transformed to the disk-frame along the emission surface $z_m(r)$ and decomposed into concentric annuli. Each annulus includes a collection of pixel spectra with different peak velocities. The velocity v in that annulus was set to the systemic value that aligns these pixel spectra so that the width of their average (stacked) spectrum is minimized (`fit_method='dV'`; Teague et al. 2018). Each annulus is considered independently to build up a realization of the profile $\{r, z_m, v, \delta v\}$ for each **Layer 3** draw.

Each extracted velocity profile is then interpreted in the context of the model for the velocity field,

$$v_m(r, z, \theta_4) = v_\phi(r, z_m), \quad (28)$$

as defined in Eq. (10) and the rest of Section 2.2, where $\theta_4 = [M_*, M_d, p, \gamma, r_t, f_{\text{vphi}}]$. The (log-)likelihood function $\ln \mathcal{L}_4 = \ln \mathbf{p}(\{r, z_m, v, \delta v\} | \theta_4)$ was defined as

$$\ln \mathcal{L}_4 = -\frac{1}{2} \sum_i \left[\frac{(v(r_i) - v_m(r_i, z_m))^2}{s_i^2} + \ln 2\pi s_i^2 \right],$$

$$\text{with } s_i^2 = \delta v(r_i)^2 + f_{\text{vphi}}^2 v_m(r_i, z_m)^2, \quad (29)$$

where f_{vphi} is a nuisance parameter to account for any under-estimated scatter, and there is implicit conditioning on $\{\theta_1, \theta_2, \theta_3\}$ (the θ_3 contribution is subtle, but it helps set the density vertical distribution and therefore

Table 2. $\tau_{\text{los}} = 2/3$ Surface Parameters, θ_2^*

	z_0 (au)	φ	r_z (au)	ψ
model A	43	1.07	323	3.99
model B	43	1.06	309	6.51
model C	42	1.05	313	10.61

the kinematic deviations associated with ε_p). As in the previous layers, for each $\{\theta_1, \theta_2, \theta_3\}$ draw and associated $\{r, z_m, v, \delta v\}$, the (log-)posterior distribution

$$\ln \mathbf{p}(\theta_4 | \{r, z_m, v, \delta v\}) \propto \ln \mathcal{L}_4 + \ln \mathbf{p}(\theta_4) \quad (30)$$

was sampled, and then the N_3 sets of those samples were combined into a final über-set.

5. KINEMATICS ANALYSIS: RESULTS

Acknowledging that the hierarchical inference strategy outlined above seems (perhaps unpleasantly) complicated, this section guides the reader through various assumptions to demonstrate how the different aspects of the procedure work and how certain factors contribute to the precision and accuracy of the key parameters.

5.1. Spatial Resolution Bias

We start with some direct ‘fidelity’ tests of the modeling infrastructure, vastly oversimplifying the parameter-space by assigning δ -function priors at the input values (denoted with asterisk superscripts): $\mathbf{p}(\theta) = \delta(\theta - \theta^*)$. Such priors apply to all parameters except the subset of θ_4 comprising $[M_*, M_d]$ (and f_{vphi}). This means we effectively skipped over **Layers 1–3** in the hierarchy. The primary goal is to illustrate that bias enters the problem even in such an (unrealistic) omniscient state.

First, we need to establish the true emission surface parameters θ_2^* : unlike all the other parameters, θ_2 are not explicitly specified. We used the `tausurf` mode of raytracing in `RADMC-3D` to generate cubes of the disk-frame coordinates (r, ϕ, z) where the line-of-sight optical depth $\tau_{\text{los}} = 2/3$ (i.e., using the Eddington approximation to define the photosphere). We associated the surface with the coordinates that correspond to the frequency of peak emission in each pixel. Since the line emission is so optically thick, these surfaces trace the tops of the CO-rich layers ($z_m(\theta_2^*) \approx z_{\text{crit}}$ in Eq. 17), as was assumed above (e.g., in making Figure 5). Table 2 compiles the results for each fiducial model.

With the priors set (to the values in Tables 1 and 2), we performed the **Layer 4** extractions of velocity profile data for the raw, sampled, and noisy cubes. We adopted radial bins spaced by $0''.05$ (roughly half the synthesized beam FWHM) and extending out to where the line intensity is below the noise floor. Figure 11 shows the extracted velocities for each cube type and fiducial model,

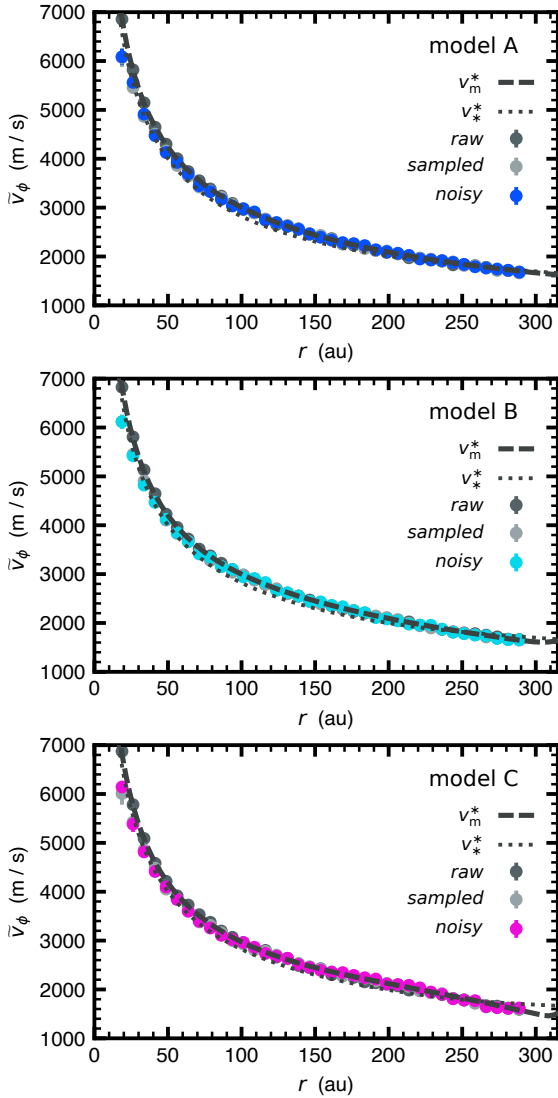


Figure 11. The extracted $\tilde{v}_\phi(r)$ profiles from the raw, sampled, and noisy versions of each model cube, compared with the true model $v_m^*(r)$ and the “background” field set by the stellar potential, $v_*^*(r)$ along the emission surfaces (Table 2). Notice how the extracted $\tilde{v}_\phi(r)$ profiles from cubes with limited spatial resolution (sampled and noisy) are systematically biased low (by $\lesssim 10\%$) in the inner disk ($r \lesssim 100$ au).

compared with the associated true profiles (v_m^*) and the contributions from the stellar potential alone (v_*^*).

Overall, the extracted velocities $\tilde{v}_\phi(r)$ match the true profile well, recovering the behavior of the subtle residuals induced by pressure support and self-gravity across most of the disk. But at smaller radii ($\lesssim 100$ au), the extractions from the sampled and noisy cubes are biased low. This is an artifact of the spatial resolution: it is a consequence of the beam-averaging of gradients in the projected intensity distribution (e.g., see [Keppler et al. 2019](#) or [Boehler et al. 2021](#)). Those intensity gradients

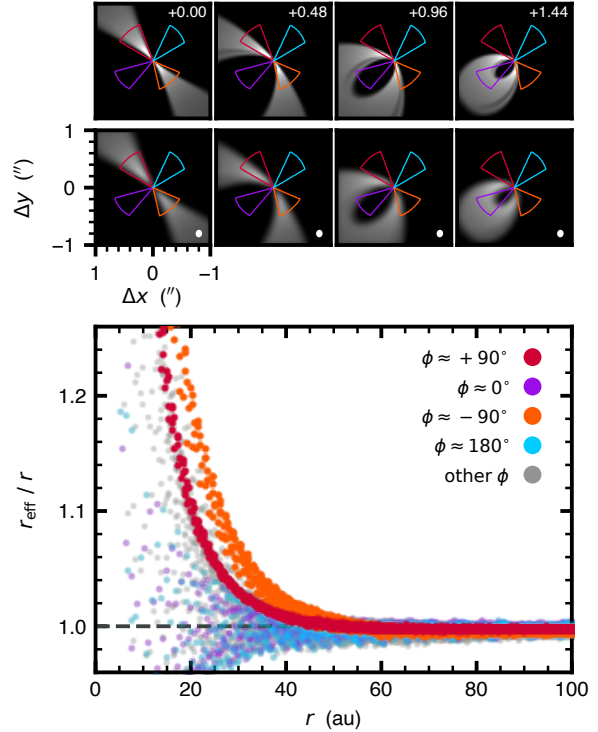


Figure 12. The top rows show a small subset of channel maps for the model B raw cube (top) and the raw cube convolved with a Gaussian kernel matched to the synthesized beam (marked in the lower right corners), appropriate for the sampled (and noisy) cube. These show every sixth 80 m s^{-1} channel to span a broader (projected) spectral range, with LSRK velocities (in km s^{-1}) marked in the upper right corners of the top row. The bottom plot shows the ratio r_{eff}/r for all pixels, color-coded by some representative azimuthal ranges (as marked in the channel maps). This highlights that the beam-averaged intensity distributions in the inner disk generally behave like the pixels from larger radii, and thereby will have effective velocities that are biased low. There is a complex azimuthal behavior, however, which means that a direct analytic correction is a challenge. Instead, we adopted an empirical correction process that works sufficiently well.

are most pronounced in the channel maps at small radii (and compact line wings). Spatial filtering (limited u , v -coverage) has negligible contribution here: the bias for the sampled cube is nearly identical to that measured from convolving the raw cube with a Gaussian beam. However, sparse spatial frequency sampling might produce an analogous bias in less ideal datasets.

Figure 12 illustrates the origins of this resolution bias. In terms of extracting $\tilde{v}_\phi(r)$ from a cube, the *effective radius* (r_{eff}) of each pixel can be approximated with the average of the true r in each pixel weighted by the intensity distribution. For the raw cube (top row), the pixels are independent and there is no bias: $r_{\text{eff}} = r$, the true projected radius in the disk-frame along the emission

surface z_m^* (Table 2). But when we convolve the raw cube with a Gaussian beam (matched to the synthesized beam for the sampled cube; next row in Fig. 12), the beam-averaged intensities from neighboring pixels factor into the averages. At larger r , the convolved intensity gradients on beam scales are modest, so $r_{\text{eff}} \approx r$. But at smaller r , there are steeper intensity gradients present on sub-beam scales that generally push $r_{\text{eff}} \gtrsim r$. The bottom panel of Figure 12 demonstrates this effect. While there is a complicated azimuthal dependence, the net impact is clear: limited spatial resolution makes the properties of the emission in these regions behave like they originate at larger radii, which (given the velocity gradient) translates into a bias to diminished $\tilde{v}_\phi(r)$.

It is hard to predict where and how this effect becomes problematic in general, since it depends on a non-trivial combination of the disk velocity field, viewing geometry, and resolution. But this bias is a significant concern at radii well beyond the resolution scale, extending here to $\gtrsim 4\times$ the synthesized beam FWHM. Moreover, the bias is independent of the $\tilde{v}_\phi(r)$ extraction algorithm: it is an intrinsic property of the data, and will be an issue for any approach that does not forward-model the effects of limited spatial resolution. As we demonstrate below, this bias needs to be corrected upon extraction to avoid propagating it into the **Layer 4** inference.

Fortunately, a straightforward (if crude) debiasing approach works well. Assuming the bias is produced solely by these beam-smearing effects, a radial profile of correction factors $C_v(r)$ can be determined empirically by comparing velocity extractions from *similar* mock data with known velocity fields and intensity gradients. For each dataset, we used `csalt` (Andrews et al., *in preparation*) to generate a mock cube with the same pixels and channels and the median extrinsic properties determined in **Layer 1**. The mock cube assumed the emission originates in a thin layer defined by the median $z_m(r)$ inferred in **Layer 2**, with a power-law brightness temperature profile set to the median $T_m(r)$ along that surface inferred in **Layer 3**. We assumed linewidths were thermal, and optical depths were high (1000 at 150 au) and decreased inversely with r (although those two assumptions are less important here). The mock velocity field was set to $v_\phi^{\text{mock}} = v_*^{\text{mock}}(M_*)$ (Eq. 11) along the emission surface, with M_* assigned based on a least-squares fit to the median $\tilde{v}_\phi(r)$ extracted from the dataset. The mock cube was then convolved with a Gaussian kernel matched to the synthesized beam. We then followed Section 4.4 and extracted N_3 realizations of $\tilde{v}_\phi^{\text{mock}}(r)$ from the mock cube using the $\{\theta_1, \theta_2, \theta_3\}$ draws determined from the data (the noisy cubes) in **Layer 4**.

We defined the correction factors as

$$C_v(r) = \frac{v_*^{\text{mock}}(r)}{\tilde{v}_\phi^{\text{mock}}(r)}, \quad (31)$$

the ratio of the input velocities to the (beam-convolved, biased) extracted values for the mock cube. The $C_v(r)$

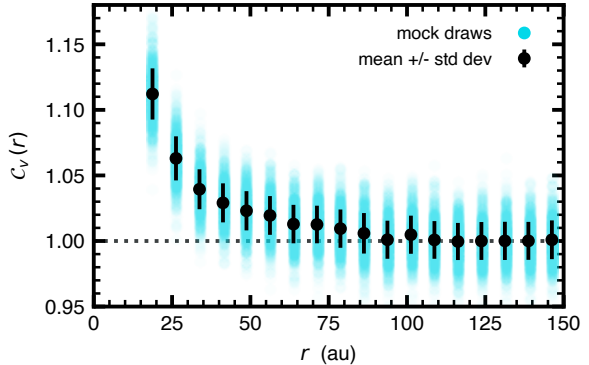


Figure 13. The velocity correction factors measured empirically for model B using $N_3 = 2,000$ extractions from a (convolved) mock cube. The averages over all mocks in each radial bin were adopted to adjust for the resolution smearing effect that biases the extracted velocities at smaller r .

measured from the mocks for model B are shown in Figure 13. The $C_v(r)$ are indistinguishable for the three fiducial models and relatively insensitive to uncertainties in the input parameters (within $<1\%$ standard deviations), confirming the basic assumption that beam-smearing of the projected spatio-kinematic field (scaling with the same, well-constrained factor $\sqrt{M_*} \sin i$) is the origin of the bias. From this point, we consider the **Layer 4** “data” as the *bias-corrected velocities* (based on the correction factors derived from the mocks), defined as $v_\phi(r) = \overline{\tilde{v}_\phi(r)} C_v(r)$ (the overline denoting the average over the mocks; e.g., the black points in Figure 13).

With those considerations, we performed the **Layer 4** inference in the special case where $\theta_1, \theta_2, \theta_3$, and the $\Sigma(r)$ parameters p, γ, r_t are fixed at their true values. We adopted uniform priors for the limited subset of θ_4 ,

$$p(\theta_4) = \begin{cases} p(M_*) \sim \mathcal{U}(0, 5 M_\odot) \\ p(M_d) \sim \mathcal{U}(0, 1 M_\odot) \\ p(\ln f_{\text{vphi}}) \sim \mathcal{U}(-10, 2). \end{cases} \quad (32)$$

We configured a standard `emcee` setup to have 64 walkers, initialized by random draws from the priors. Here, we sampled the posteriors for 10,000 steps and assessed convergence based on the autocorrelation times (τ) (in this case ~ 50 steps). We discarded the initial $20\langle\tau\rangle$ steps (as the burn-in phase) and thinned by retaining every $0.5\langle\tau\rangle$ step from the remaining samples for each walker. Figure 14 shows the results of those inferences, comparing the *residual* velocity profiles (defined here by reference to the true stellar potential profile, $\Delta v_\phi = v_\phi - v_*^*$, solely for ease of visualization; note the actual quantity used in the inference calculations is v_ϕ) with posterior draws for the raw, sampled, and noisy cubes of each model. The marginalized posterior distributions for M_* and M_d are presented to the right in each row. The estimated uncertainties from the profile extractions (δv) are

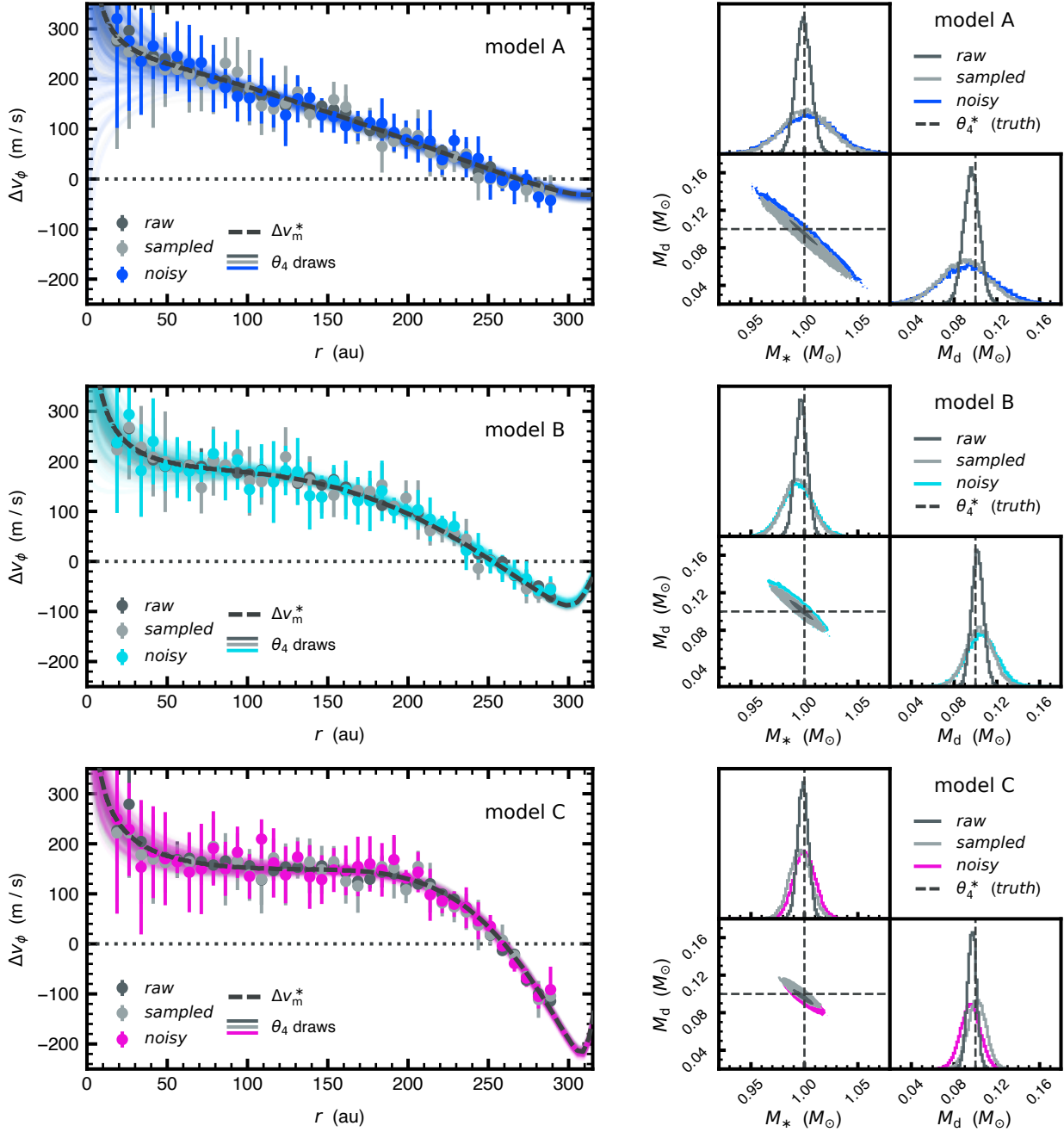


Figure 14. (*left*) The extracted (and bias-corrected) residual velocity profiles, referenced to the true stellar potential profile, $\Delta v_\phi = v_\phi - v_*$, from the raw, sampled, and noisy cubes for each fiducial model. These are compared with the true profile along the emission surface (Δv_m^*) and profiles constructed from 100 random draws of the posteriors inferred assuming δ -function priors for θ_1 , θ_2 , θ_3 , and the $\Sigma(r)$ parameters set at their true values, and the M_* and M_d priors in Eq. (32). (*right*) The marginalized posteriors, with the true values marked with dashed lines (contours mark the 2σ confidence intervals).

appropriate: no evidence for inflated scatter was found ($f_{\text{vphi}} < 0.009$ at 99% confidence).

The inferences for all cube types overlap well, with peaks that recover the true M_* well within 1% and only modest ($\lesssim 10\%$) biases on M_d , along a clear degeneracy (anti-correlation). This is the accuracy limit induced by

the procedure outlined in Section 4.4, at least in this specific case of rigid model restrictions. Note that the inferred precision improves for steeper $\Sigma(r)$ tapers, because it is easier to differentiate pressure support and self-gravity when the kinematic impact of the taper is

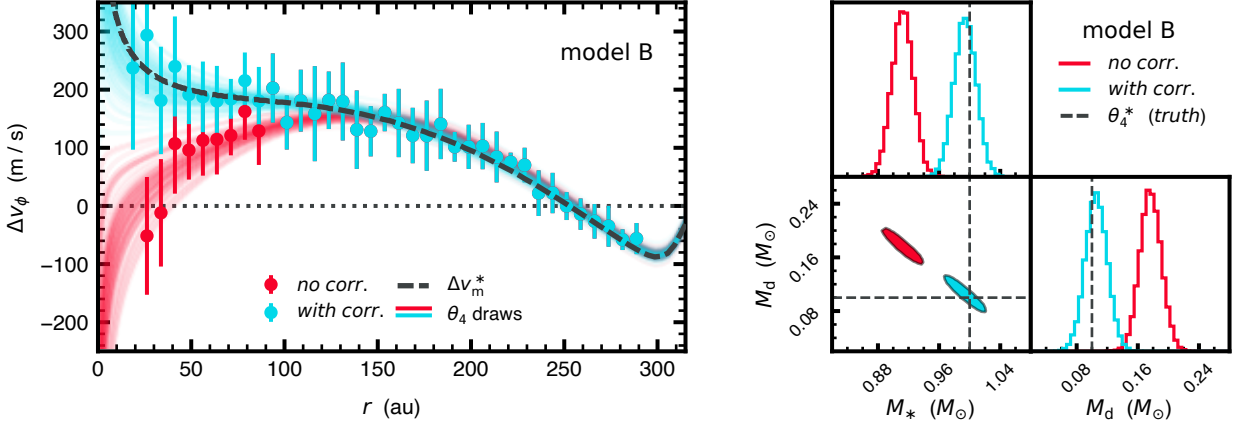


Figure 15. A comparison of variations on the extracted (residual) velocities for the **model B** noisy cube and their influence on the inferences of M_* and M_d , following the same prescription and notations as in Figure 14. These include the *uncorrected* $\tilde{v}_\phi(r)$ (red) and the *corrected* $v_\phi(r)$ (blue: the same as in Figure 14). The limited spatial resolution of the data biases the extracted velocities low, out to a radius much larger than the synthesized beam FWHM. Those artificially diminished velocities (red) produce substantial biases in the physical parameters of interest. An approximate empirical correction, derived presuming that the projected velocity field is biased by beam convolution, substantially mitigates those inaccuracies (blue).

confined to a narrow radial range (e.g., ~ 230 – 280 au for **model C**, compared to ~ 75 – 280 au for **model A**).

Before relaxing the modeling restrictions imposed by the strict priors, it is instructive to more directly illustrate the effects of the resolution bias noted above. Figure 15 compares the results of inferences for the **model B** noisy cube using either the *uncorrected* $\tilde{v}_\phi(r)$ (red) or the *corrected* $v_\phi(r)$, as in Figure 14 (blue). The resolution bias imparts significant biases on M_* and especially M_d , pushing the posteriors along their covariance to lower M_* ($\sim 10\%$) and higher M_d ($\sim 170\%$). The stellar potential (v_* term in Eq. 10) is more important in the inner disk, so the resolution bias to lower v_ϕ at small r pushes the M_* inference lower. To compensate for the reduced velocities at larger r , where self-gravity is important, the inferred M_d is pushed higher. The amount of bias depends on the $\Sigma(r)$ taper: it is more problematic for lower γ , where the taper affects a larger radial range (**model A**). Ignoring a correction for this resolution bias will deliver misleading M_d measurements.

5.2. Geometry and Surface Effects

Next, we explore the downstream effects that are associated with precision and accuracy in the geometry (**Layer 1**) and emission surfaces (**Layer 2**). Like Section 5.1, we set δ -function priors at the true values for θ_3 (skipped **Layer 3**) and a subset of θ_4 (p , γ , and r_t). In **Layer 1**, we drew $N_1 = 500$ samples from θ_1 “posteriors” that we *assigned* – in practice, this means drawing from adopted priors $\mathbf{p}(\theta_1)$. We assumed that these priors were independent and normally distributed $\sim \mathcal{N}(\mu, \sigma)$, with means set at their true values (Table 1) and standard deviations comparable to those inferred in the literature for similar targets (e.g., Huang et al. 2018a; An-

drews et al. 2021),

$$\mathbf{p}(\theta_1) = \begin{cases} \mathbf{p}(\Delta x) \sim \mathcal{N}(0.00, 0.01'') \\ \mathbf{p}(\Delta y) \sim \mathcal{N}(0.00, 0.01'') \\ \mathbf{p}(i) \sim \mathcal{N}(30, 0.5^\circ) \\ \mathbf{p}(\vartheta) \sim \mathcal{N}(130, 0.5^\circ) \\ \mathbf{p}(v_{\text{sys}}) \sim \mathcal{N}(0, 4 \text{ m s}^{-1}). \end{cases} \quad (33)$$

These θ_1 draws were used to extract N_1 sets of surface coordinates $\{r, z, \delta z\}$ in **Layer 2**.

We then inferred θ_2 posterior samples for each draw, adopting uniform priors for the surface parameters,

$$\mathbf{p}(\theta_2) = \begin{cases} \mathbf{p}(z_0) \sim \mathcal{U}(0, 150 \text{ au}) \\ \mathbf{p}(\varphi) \sim \mathcal{U}(0, 5) \\ \mathbf{p}(r_z) \sim \mathcal{U}(0, 450 \text{ au}) \\ \mathbf{p}(\psi) \sim \mathcal{U}(1, 15), \\ \mathbf{p}(\ln f_{\text{surf}}) \sim \mathcal{U}(-10, 2). \end{cases} \quad (34)$$

The θ_2 posteriors were sampled with **emcee**, using 64 walkers for 10,000 steps. The mean autocorrelation time for those samples was $\langle \tau \rangle \approx 60$ steps. The mean value of the nuisance parameter $f_{\text{surf}} \approx 1$, indicating the surface uncertainties (δz) are under-estimated by a factor ~ 5 – 10 (as expected, given the large scatter found for any individual extracted set of surface coordinates).

Figure 16 summarizes the emission surface inferences in **Layer 2**. The θ_2 posteriors produce $z_m(r)$ that mimic the shape of the true surface, but are systematically low (a mean offset $\Delta z/r \approx -0.05$). That bias is caused by two factors. First is a radiative transfer effect (diagnosed

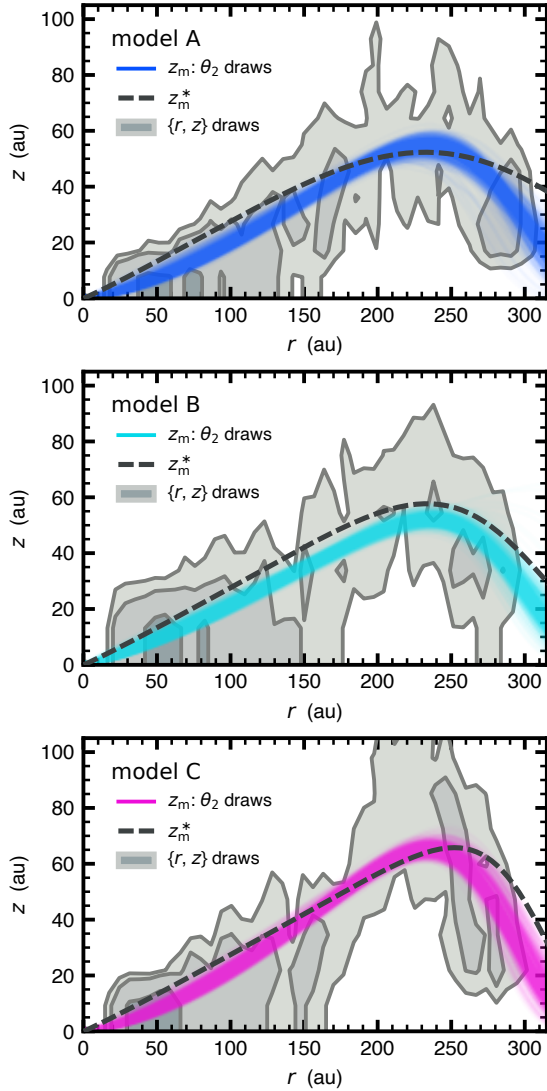


Figure 16. Histogram summaries of the extracted surface coordinates $\{r, z\}$ for the noisy cubes of each fiducial model (contours mark 15, 50, and 85% of the coordinates) from the N_1 realizations in **Layer 2**, compared with the z_m profiles from 1,000 draws of the θ_2 posteriors and the true z_m^* profiles.

with the raw cubes, in some experiments with the back surface removed in the **RADMC-3D** calculations), where **disksurf** finds shifted emission lobe centroids because of the asymmetric intensity “shoulders” produced over a range of line-of-sight depths into the disk. These are exacerbated for higher inclinations, thicker CO-rich layers, and steeper vertical temperature gradients. Second is a spatial resolution effect, where the emission lobe peaks become difficult to separate at smaller r .

A subset of $N_2 = 1,000$ draws from the $\{\theta_1, \theta_2\}$ posterior samples collected in **Layer 2** were propagated to **Layer 4** to extract realizations of $\{r, v, \delta v\}$. The bias-corrected $v_\phi(r)$ from this ensemble spans a range with a standard deviation that is $\sim 30\%$ larger than the for-

mal uncertainties in any individual draw (35–65 m s^{-1} compared to 25–50 m s^{-1}). That additional scatter is dominated by ambiguities in the geometric parameters; uncertainties in the emission surfaces are negligible. The mean extracted $v_\phi(r)$ is similar to the true input (v_m^*), suggesting the geometry and surface ambiguities do not impart a strong bias in the velocity extractions. Using the same **emcee** setup as in Section 5.1, we sampled the (subset of) θ_4 posteriors for each draw and combined the (burned-in, thinned) results (the mean autocorrelation time was $\langle \tau \rangle \approx 50$ steps). As before, there is no need to account for additional scatter in the velocity profile extractions ($f_{\text{vphi}} < 0.01$ at 99% confidence).

Figure 17 summarizes the (subset of) θ_4 posteriors and corresponding $v_\phi(r)$ in this case, where the θ_3 and $\{p, \gamma, r_t\}$ parameters in θ_4 are held fixed by δ -function priors at the true values. The peaks of the marginal posteriors for M_* and M_d do not shift much compared to Section 5.1 (Figure 14); the small biases noted are largely tied to the rigidity of the model given the adopted priors. This confirms that the surface bias noted in Figure 16 does not propagate into a significant v_ϕ bias. That is not surprising, since the vertical variation of the velocity field in the disk models used to generate the data are modest (Figure 4). The posterior widths for M_* and M_d broaden (roughly by a factor of two) when the geometry and surface ambiguities are considered, tracing the increased range of the extracted $v_\phi(r)$ profiles due primarily to the ambiguities in θ_1 . But we do not read too much into these posterior morphologies because the stringent priors limit the flexibility in the inference.

5.3. The Complete, Layered Inference

Having now explored the isolated consequences of the geometric and emission surface parameters, we relax the stringent constraints on the parameters describing the physical conditions (i.e., θ_3 and the rest of θ_4) and run the full hierarchical workflow (Section 4; Figure 10). Following the steps outlined above, we started from the **Layer 2** outputs and extracted $N_2 = 1,000$ realizations of the $T_b(r)$ profile corresponding to the subset of draws from the $\{\theta_1, \theta_2\}$ posterior samples.

Next, we assigned a joint conditional θ_3 prior,

$$p(\theta_3) = \begin{cases} p(T_{m,0}) \sim \mathcal{N}(45, 8 \text{ K}) \\ p(T_{a,0}) \sim \mathcal{U}(0, 400 \text{ K}) \\ p(q) \sim \mathcal{N}(0.5, 0.1) \\ p(a_z) \sim \text{Exp}(10) \\ p(w_z) \sim \text{Exp}(20) \\ p(\ln f_{\text{temp}}) \sim \mathcal{U}(-10, 2) \end{cases} \quad (35)$$

if $T_{m,0} \leq T_{a,0}$, or $p(\theta_3) = 0$ otherwise. The $\sim \text{Exp}(\lambda)$ expression for a_z and w_z in Eq. (35) denotes an exponential prior $p(x) = \lambda e^{-\lambda x}$. We adopted this form to deprioritize large values, where the prescription is problematic (the \tanh in Eq. 7 does not have finite support).

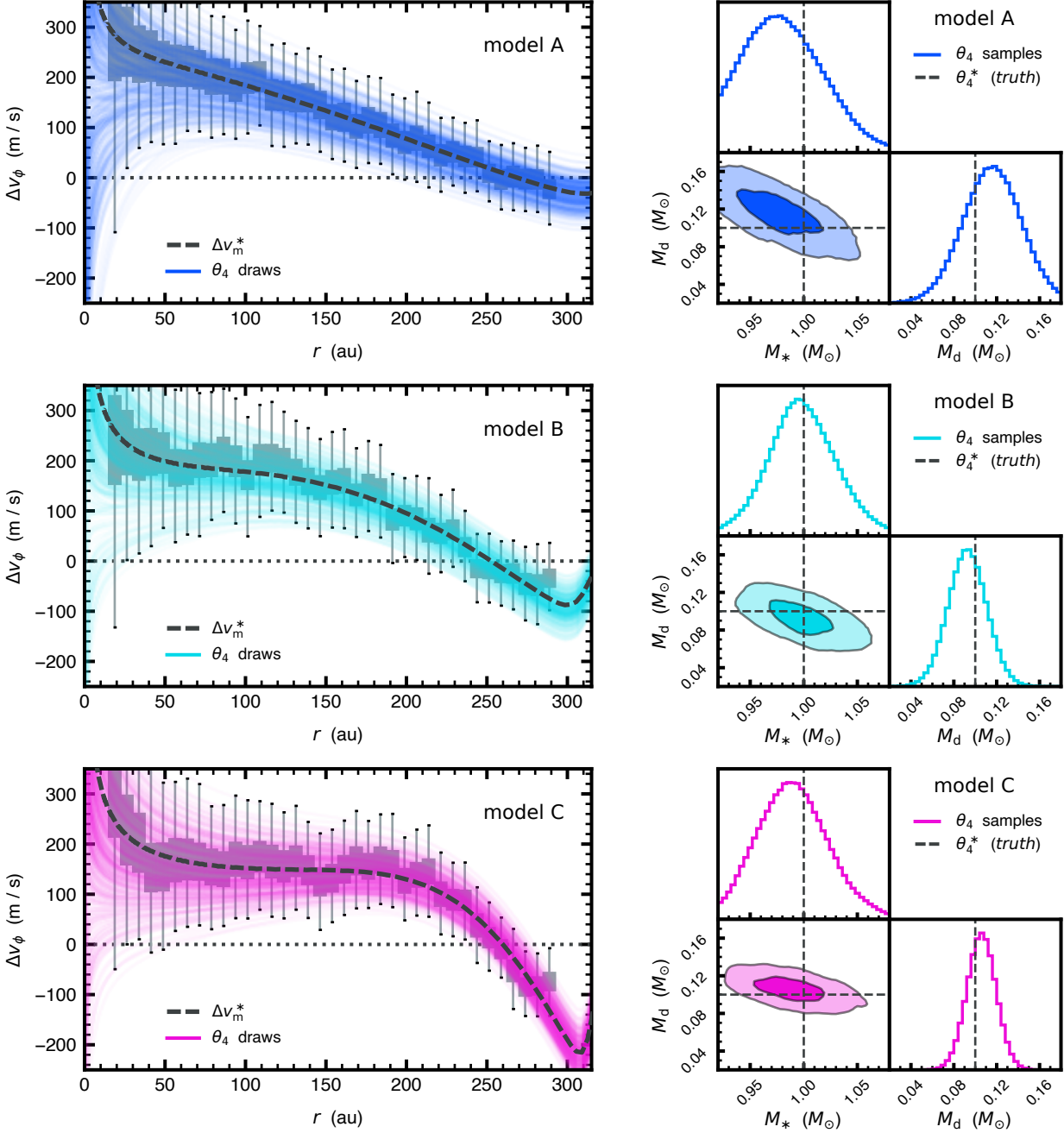


Figure 17. As in Figure 14, a comparison of the residual velocity profiles (*left*) and marginalized posteriors for the restricted model inferences (*right*), now accounting for the ambiguities in the geometry and emission surfaces. The box-whisker plots show the distributions of the velocity extractions: the boxes denote the interquartile range (50%) and the whiskers (error bars) span 99% of the extractions. The covariance corner plots show contours at the 1 and 2σ confidence intervals.

The prior for $T_{m,0}$ was assigned based on a simplified prescription for a passive irradiated disk,

$$T_{m,0} \approx \left[\frac{\eta L_*}{8\pi\sigma_{\text{SB}} r_0^2} \right]^{1/4}, \quad (36)$$

where η is the flaring angle of the disk surface, L_* is the stellar luminosity, and σ_{SB} is the Stefan-Boltzmann

constant (Chiang & Goldreich 1997; Dullemond et al. 2001). Adopting a log-normal L_* prior with a typical uncertainty (Alcalá et al. 2017) that peaks at the Baraffe et al. (2015) model value for a 1 M_\odot star at 2 Myr, $p(\log_{10}(L_*/L_\odot)) \sim \mathcal{N}(0.08, 0.15)$, and a liberal uniform prior for the flaring angle, $p(\eta) \sim \mathcal{U}(0.01, 0.1)$, the prescription in Eq. (36) suggests a $T_{m,0}$ prior reason-

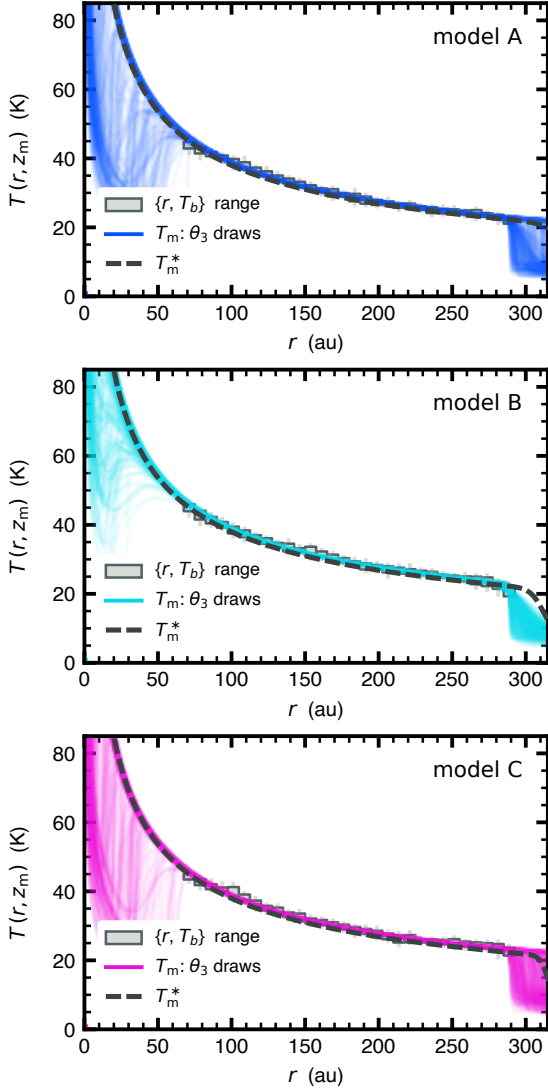


Figure 18. Summaries of the extracted $T_b(r)$ profiles from the N_3 realizations in Layer 3, compared with the reconstructed $T_m(r, z_m)$ from 500 draws of the θ_3 posteriors and the true temperature profile along the emission surface $T_m^*(r, z_m^*)$.

ably approximated with Eq. (35). Note the slight bias compared to the true value ($T_{m,0}^* = 40$ K; Table 1).

We then proceeded with the inference step in Layer 3 and sampled the θ_3 posteriors for 64 walkers and 10,000 steps (mean autocorrelation time $\langle \tau \rangle \approx 140$ steps). The additional scatter term here was small, with $f_{\text{temp}} < 0.01$ (99% confidence). Figure 18 summarizes the results: the θ_3 posteriors are somewhat biased off the true values, as expected for the very limited constraints the $T_b(r)$ profile along a single emission surface offers. The adopted priors are perhaps unfairly stringent, since they dominate the inferences for $T_{m,0}$. However, if multiple spectral line datasets can be combined, the Layer 3 inferences can be less reliant on such priors.

Next, we drew a subset of $N_3 = 2,000$ realizations of $\{\theta_1, \theta_2, \theta_3\}$ from the Layer 3 über-set of posteriors and propagated those to Layer 4 to extract N_3 velocity profile datasets $\{r, v, \delta v\}$. Each of those (bias-corrected) $v_\phi(r)$ realizations was then used to infer posterior samples for the full complement of θ_4 , again using `emcee` and 64 walkers for 25,000 steps. In addition to the priors specified in Eq. (32), we adopted

$$p(\theta_4) = \begin{cases} p(p) \sim \mathcal{U}(0, 2) \\ p(\gamma) \sim \mathcal{U}(0, 6) \\ p(r_t) \sim 1 - \text{Logistic}(300 \text{ au}, 0.1), \end{cases} \quad (37)$$

where the $\text{Logistic}(x_0, b)$ distribution is

$$p(x) = \left(1 + e^{-b(x-x_0)}\right)^{-1}. \quad (38)$$

In this case, $p(r_t)$ acts like a soft upper bound (in practice, the adopted x_0 simply means we assume the Σ taper happens at a radius where we still detect CO emission, as suggested by the $z_m(r)$ and $\Delta v_\phi(r)$ behaviors). The Eq. (37) priors are designed to be effectively agnostic. We also included a composite prior that ensures the solutions are gravitationally stable,

$$p(\min Q) = \text{Logistic}(2, 20), \quad (39)$$

with $\min Q$ the minimum Toomre parameter (Eq. 21). This prior is designed so that instability accrues a steep penalty, but stable models ($\min Q \gtrsim 2$) are equally probable. We consider this a well-motivated prior for massive, axisymmetric disks, which helps avoid artificially broadening the M_d posteriors to non-physical values. If M_d is lower, it is essentially negligible.

The Layer 4 inference results are presented in Figures 19–21, which show marginalized projections for pairs of θ_4 posterior samples along with comparisons of the extracted (residual) velocities and $\Delta v_\phi(r)$ reconstructed from random posterior draws for each fiducial model. The mean autocorrelation time was $\langle \tau \rangle \approx 200$ steps.

The inferred M_* – M_d covariance behavior is similar to what was noted for the more restricted inferences in Sections 5.1 and 5.2. However, the flexibility afforded by relaxing the priors on the θ_4 parameters that describe $\Sigma(r)$ imparts a more general complexity on the results. In all cases, the marginalized M_* and M_d posteriors are consistent with the true values: biases for these parameters are $\lesssim 2\%$ and $\lesssim 20\%$, respectively.

The precision of the M_d measurement depends on the $\Sigma(r)$ taper. Broader posteriors (less precision) are found for more gradual tapers (lower γ): the 90% confidence intervals for M_d span roughly $\pm 0.08 M_\odot$ for model A ($\gamma = 1$), $\pm 0.06 M_\odot$ for model B ($\gamma = 2$), and $\pm 0.04 M_\odot$ for model C ($\gamma = 4$). As we noted above, the underlying difference is the radial range over which the density taper matters. For steep tapers like model C, that range is

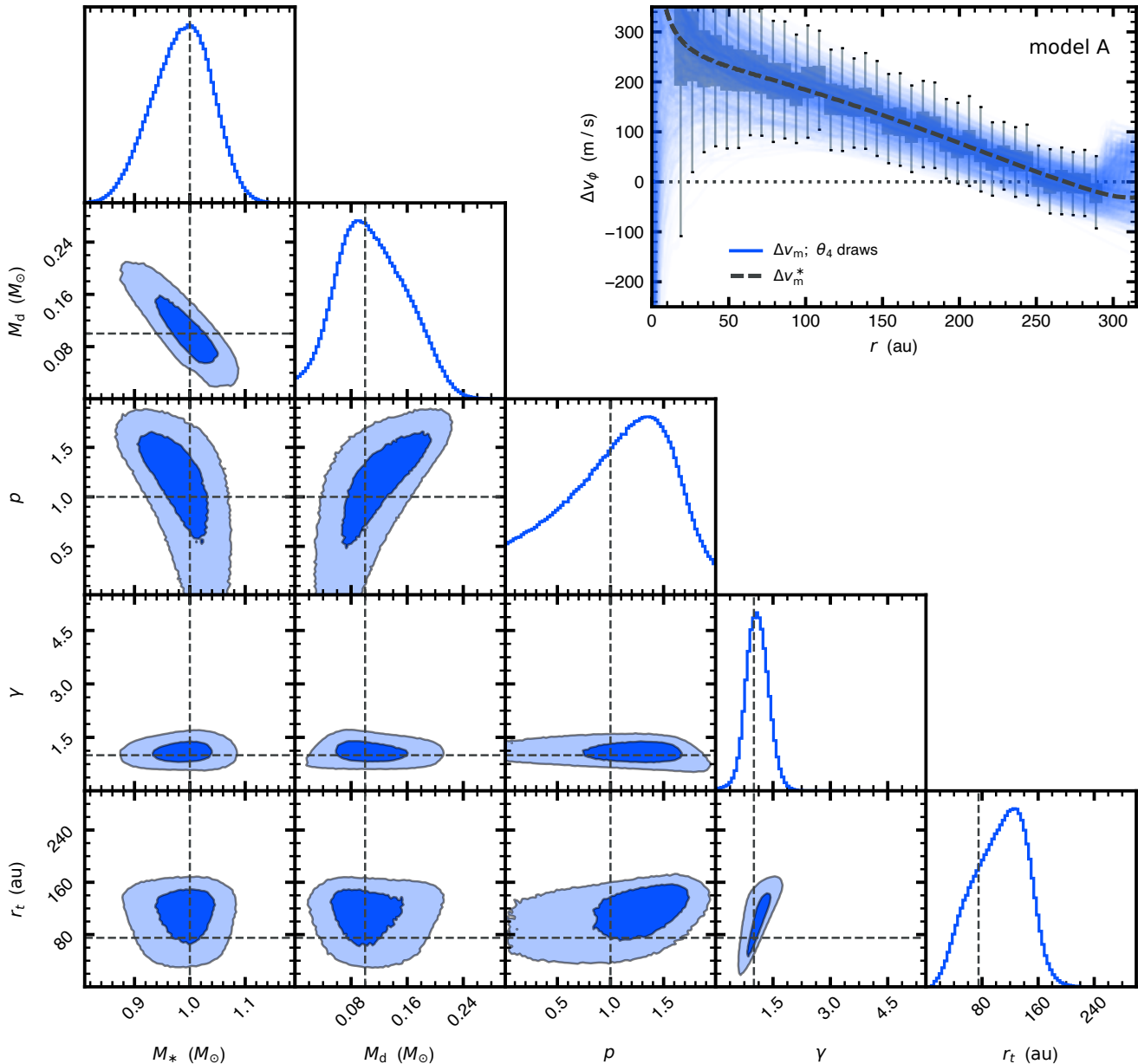


Figure 19. The marginalized θ_4 posteriors for model A, compared with θ_4^* : contours mark the 1 and 2σ confidence intervals. The panel in the upper right shows a binned summary of the extracted (residual) velocity profile data from the N_3 realizations in Layer 4 (as in Figure 17), compared with the reconstructed Δv_m from 1,000 draws of the θ_4 posteriors and the true Δv_m^* .

limited and the kinematic signature is pronounced: it is therefore easier to constrain the detailed shape of $\Sigma(r)$ from the dynamical contributions of both pressure support and self-gravity. But for gradual tapers like model A, much more of the disk is affected; this accentuates the kinematic degeneracy between ε_p and ε_g .

Despite these details, the overall quality of the surface density profile retrievals for these fiducial models – using solely the kinematics information in spectral line measurements – is remarkably good. Figure 22 shows $\Sigma(r)$ profiles reconstructed from the θ_4 posterior draws

in each case, compared with the true (input) profiles. The bulk of the posterior draws find $\Sigma(r)$ profiles within a factor of two of the true profiles over essentially the full range of radii that produces CO line emission.

6. DISCUSSION

6.1. Applicability and Limitations

Considering the analyses presented in Section 5 holistically, a few important lessons can be distilled from this methodological study. First, it is essential to account for the resolution bias that impacts velocity profile extrac-

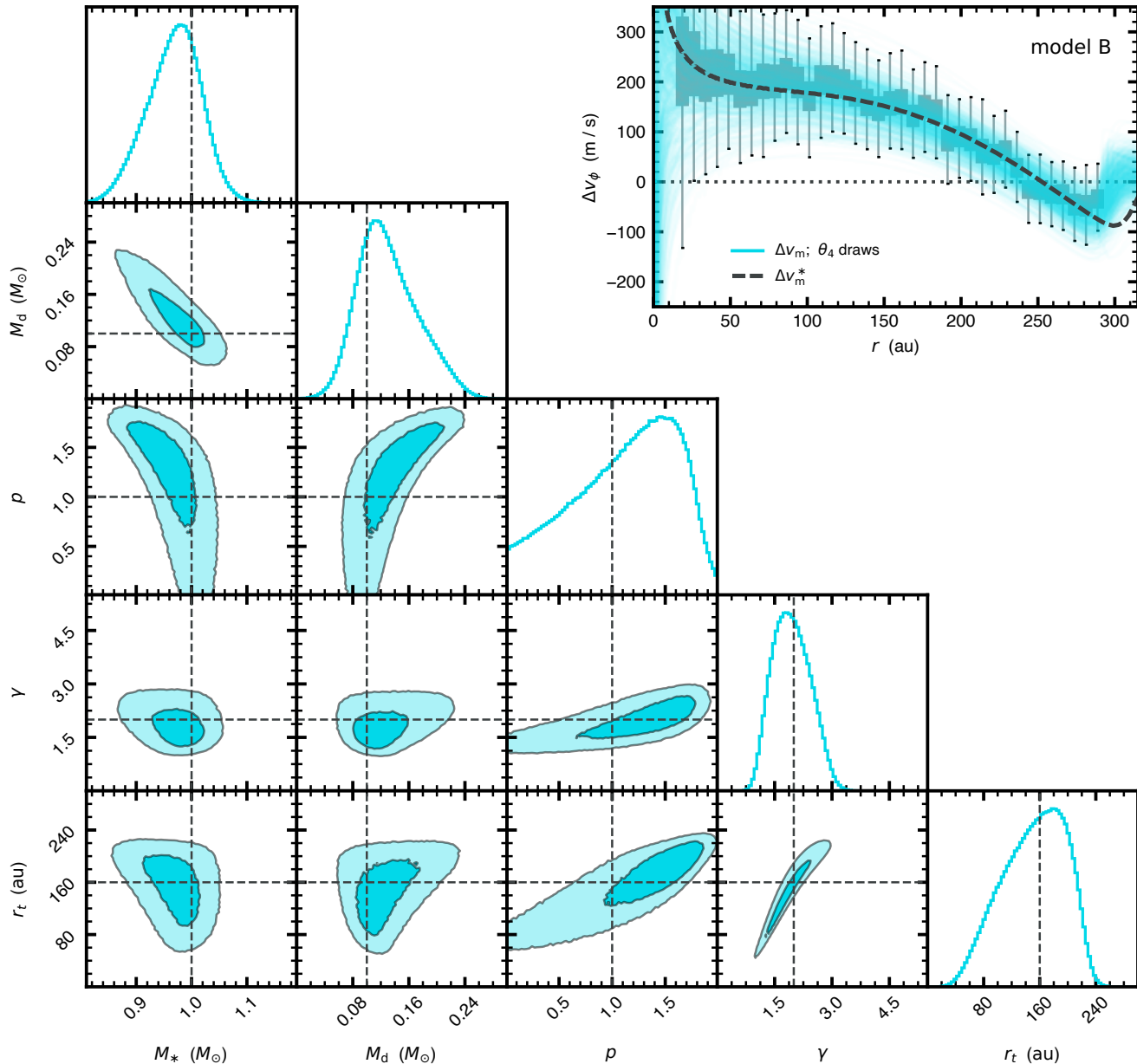


Figure 20. The same information and annotations as in Figure 19, in this case for model B.

tions at small radii to retrieve an accurate assessment of the mass distribution (Sect. 5.1): ignoring this effect injects a factor of \sim two bias (high) in the density normalization (M_d), which will unfortunately compound with other factors to undermine the effort. Second, assuming unbiased estimates of the geometric parameters, accounting for a reasonable level of ambiguity in the emission surfaces does not bias the kinematics: the typical levels of geometric uncertainty introduce only modestly degraded precision for the density inferences ($\sim 50\%$ in M_d ; Sect. 5.2). Third, intrinsic degeneracies regarding the shape of $\Sigma(r)$ are the determining factor for the qual-

ity of M_d inferences (Sect. 5.3), with less precision for gradual outer disk tapers (i.e., lower γ).

Using the layered analysis strategy developed for this task (Sect. 4), we found that we could infer $\Sigma(r)$ with remarkably good fidelity (i.e., within a factor of two) for data of appropriate quality and reasonable assumptions if the disk is an appreciable fraction of the total mass, $M_d/M_* \approx 10\%$ (Fig. 22). As that ratio decreases, the kinematic signature from ε_g decreases and the quality of the M_d retrieval is diminished. To explore that behavior, we generated a suite of analogous synthetic data for variants of model B with $M_d = 0.04, 0.06, 0.08,$ and $0.12 M_\odot$. Aside from scaling the column density threshold

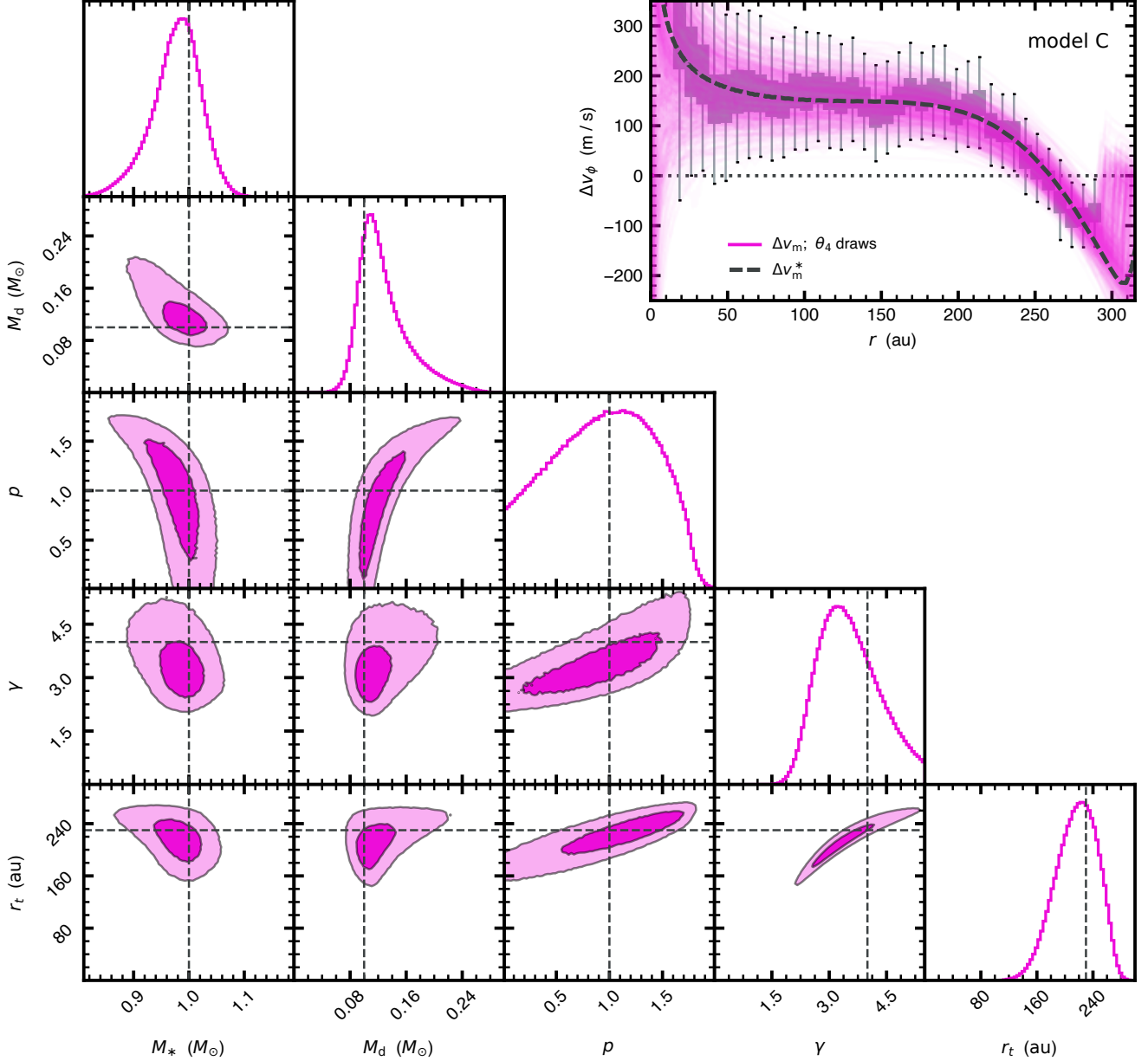


Figure 21. The same information and annotations as in Figure 19, in this case for model C.

for the upper boundary of the CO-rich layer (σ_{crit}) to compensate for the different M_d and maintain a fixed emission size, the other input parameters were fixed to the values in Table 1. We followed the same full inference procedure as above for each of these variants. The marginalized M_d posteriors for each (including the fiducial model B) are shown together in Figure 23, with each distribution normalized relative to the true mass.

The distributions in Figure 23 illustrate the anticorrelated behavior: the M_d posteriors broaden as the intrinsic mass ratio decreases. If all else is equal, and these models are representative, this experiment suggests that the approach outlined here could deliver good quality

M_d inferences down to $M_d/M_* \approx 5\%$ without any additional modifications. At face value, this suggests the approach may only be relevant at the high end of the M_d distribution. But recall that spectral line *intensity*-based M_d estimates at such high values struggle with accuracy, due to the high optical depths: in that sense, the kinematics approach is a valuable complement.

There are opportunities to improve this M_d sensitivity range by combining observations of the kinematics from multiple spectral lines. The intrinsic degeneracies in the problem are diminished with increasing precision in the extracted $v_\phi(r)$ information. Even if it proves difficult or impractical to seek such improvements for any given

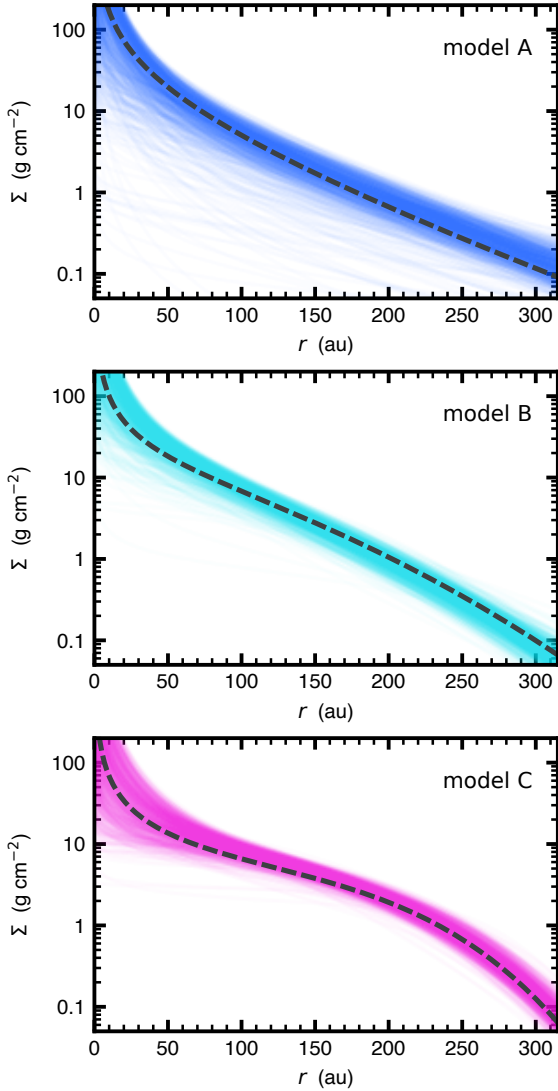


Figure 22. The reconstructed surface density profiles using 1,000 draws from the θ_4 posteriors for each fiducial model, compared with the true profiles (dashed).

spectral line, the framework described above (Sect. 4) can accommodate multiple lines that, when considered together, improve the inference quality. In practice, the multi-line approach would proceed the same way in **Layer 1** (since the disk has only one relevant set of geometric parameters), and then independently for each line in **Layer 2** and for the extraction components of **Layers 3 and 4**. But the inference components of these latter two layers would be conducted jointly for the set of lines (with simple composite posteriors).

In the simplest scenario where statistical noise dominates (rather than systematics; see below), combining N lines with similar $v_\phi(r)$ quality could yield \sqrt{N} improvement in M_d precision (e.g., a $M_d/M_* \approx 3\text{--}4\%$ measurement for two tracers). A reasonable option might be to use multiple CO transitions (e.g., CO $J=2-1$ and

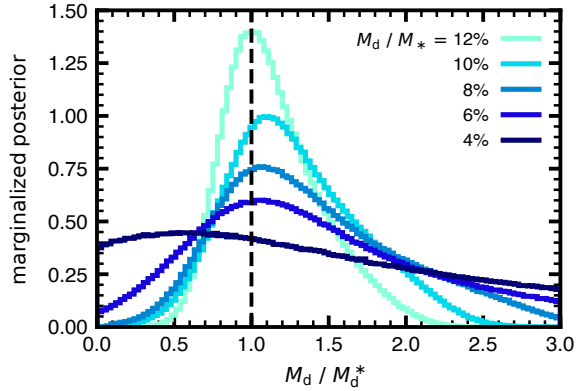


Figure 23. The marginalized M_d posteriors inferred for a sequence of model B variants with different M_d/M_* values (note that the 10% case is the fiducial model B case), following the procedure outlined in Section 4. Each distribution is normalized by the true M_d , to highlight the level of posterior broadening as the mass decreases. The transition from a firm measurement (with good fidelity) to an upper limit occurs around $M_d/M_* \approx 5\%$ in this example.

$J=3-2$) and/or another species with bright and optically thick lines (e.g., HCO^+). This might *underestimate* the improvement in the case where multiple lines probe the kinematics at sufficiently different vertical surfaces, since two-dimensional information better disentangles the contributions of pressure support and self-gravity. This is more of a challenge, but could be realized using, e.g., lines from CO isotopologues. Realistically, such lines will have less precise $v_\phi(r)$ (they are intrinsically fainter) over a more limited radial range. Nevertheless, the returns on folding in constraints with such complementary information, even if the quality is lower, would certainly benefit the $\Sigma(r)$ inferences.

6.2. Caveats and Potential

While it is difficult to properly generalize the applicability of the results for a few fiducial models to the high-dimensional parameter space (geometric, physical, observational) that may be relevant for real measurements, there are some intrinsic aspects of the problem that can guide future expectations and strategies.

From an observational perspective, while both sensitivity and spectral resolution are relevant for precision, it is especially important to *spatially* resolve the emission well. Perhaps it is obvious from the discussion of the resolution bias (Sect. 5.1), but proper sampling of $v_\phi(r)$ gradients is essential for an accurate inference of $\Sigma(r)$. As a crude reference metric, we suggest seeking $\gtrsim 20$ FWHM resolution elements across the emission distribution diameter. For this reason, it will be difficult to measure a robust $\Sigma(r)$ with this technique for compact disks (emission line radii $\lesssim 1''$) with ALMA.

We argued in Section 5.2 that the intrinsic ambiguities in our knowledge of the extrinsic geometric parameters

of a disk target (θ_1) make a substantial contribution to the scatter in the extracted $v_\phi(r)$, and therefore into the precision of the $\Sigma(r)$ inferences. It does not seem likely that we could improve measurements of the disk center or sky-projection angles much beyond what is assumed here before other systematic factors (e.g., asymmetries) dominate. However, the modeling procedure does depend on the *value* of the inclination angle (and not just the associated precision). For moderate i (~ 20 – 50°), we can do a reasonable job of inferring the emission surfaces and extracting good-quality $v_\phi(r)$, as described here. At more face-on orientations, the surfaces become more ambiguous (e.g., Teague et al. 2022), and therefore the accuracy of the $\Sigma(r)$ inferences depend more on the priors. At higher i , the $v_\phi(r)$ extractions might suffer confusion associated with the three-dimensional emission geometry (e.g., contamination from the back-side emission surface). The tradeoffs associated with the viewing geometry are complex, but will be essential to explore as the tools associated with these quantitative dynamical inferences are developed further.

Aside from acquiring suitable data, there are some areas for immediate progress that can improve $\Sigma(r)$ inferences in this analysis framework. For example, these measurements depend on a robust constraint of the two-dimensional thermal structure determined by combining optically thick tracers that sample different vertical layers (Law et al. 2021a; Paneque-Carreño et al. 2023). But in practice, we usually reconstruct a temperature distribution from sparsely sampled (in z) information. Efforts to design a better-informed, empirical prescription for $T(r, z)$ using more tracers would retire a lingering risk of biased interpretations of the kinematics. There are also potential improvements available from fine-tuning the algorithms used in extracting the emission surfaces and velocity profiles; for example, by selecting optimizers or prescriptions that are better aligned with realistic emission distributions (i.e., informed by radiative transfer simulations). If such adjustments reduce bias or improve precision – particularly in $v_\phi(r)$ – we would see strong returns on the quality of $\Sigma(r)$ inferences.

The over-arching aspiration for treating such *solvable* issues is to position the problem so that the systematics are dominated by *physical* characteristics; i.e., a mis-specification of the correct model, not some technical issue in the practical aspects of the measurements. Such mis-specification systematics could arise from complications to the analysis if various assumptions are incorrect. While many options are possible, most of the problems can be traced back to over-simplified prescriptions for the physical conditions and/or dynamics. Such incomplete parameterizations can bias the kinematic inferences in a way that is difficult to foresee. While this is a generic concern for most astronomical inference problems, there is evidence for specific examples that could prove to be subtle challenges for future work.

An obvious example is the prevalence of substructures, thought to trace localized gas pressure deviations (e.g., ALMA Partnership et al. 2015; Andrews et al. 2016, 2018; Huang et al. 2018b; Long et al. 2018). If such features are unresolved and axisymmetric, the accompanying kinematic deviations (ε_p) are likely negligible; if they are resolved, they should be incorporated into the model (by modifying the Σ and T prescriptions accordingly). But if any substructures are non-axisymmetric (e.g., spirals, vortices), the azimuthal averaging used in this analysis framework *will* generate artificial $v_\phi(r)$ structures that can bias the M_d inference: an alternative approach is required. Another, more subtle, example is the contribution of magnetic pressure. Some simulations predict that it could dominate the thermal pressure at $z/r \gtrsim 0.3$ (Hirose & Turner 2011; Wang et al. 2019), and therefore influence the kinematics (through ε_p) traced by spectral lines emitting from such heights.

In terms of the dynamics more specifically, there are various mechanisms that could introduce radial (e.g., accretion flows; Rosenfeld et al. 2014; Pérez et al. 2015) or vertical (e.g., winds or outflows; Teague et al. 2018; Galloway-Sprietsma et al. 2023) contributions to the gas motions. These were neglected here, under the assumption that they can be accurately disentangled from $v_\phi(r)$. However, this may not be the case in general, particularly for disks with complicated geometric projections (e.g., warps; Rosenfeld et al. 2012; Casassus et al. 2018). While the spectral line kinematics offer unique opportunities to probe these effects, it remains to be seen what level of bias such systematics can have on dynamical M_d estimates.

6.3. Demonstration with ALMA Data: MWC 480

Having further developed and quantitatively validated the analysis procedure outlined in this article in a ‘controlled’ environment, it makes sense to deploy it on real observations as a test case where the true disk properties are not known a priori. For this, we selected the ALMA observations from the MAPS project (Öberg et al. 2021) of the MWC 480 disk. This target has a similar geometry and CO emission surface to the fiducial models explored above (Law et al. 2021a), appears to be axisymmetric (Teague et al. 2021), and does not suffer foreground or environmental contamination (unlike, for example, AS 209 or GM Aur). Moreover, the MAPS data and the MWC 480 disk have some qualities that can help us illustrate some potential future development of the standard approach outlined in this article. We considered the cubes for the ^{12}CO and ^{13}CO $J=2-1$ transitions provided by MAPS, created with FWHM synthesized beam dimensions $0''.17 \times 0''.12$ ($\text{PA} = 6^\circ$) and a channel spacing of 200 m s^{-1} (these are the `robust = +0.5`, primary beam-corrected cubes).

The geometric parameters used in `Layer 1` were determined from the MAPS 225 GHz continuum visibilities, following the approach of Andrews et al. (2021) and

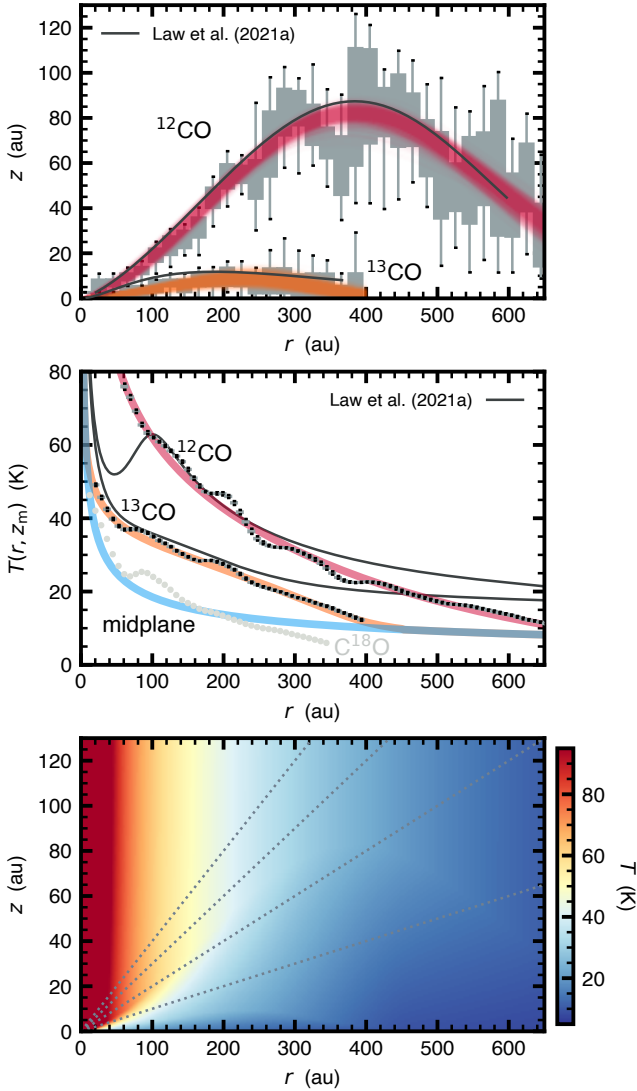


Figure 24. (*top*) The extracted (gray box-whisker plots) and inferred (colored curves) emission surfaces for ^{12}CO and ^{13}CO $J=2-1$ in the MWC 480 disk. Black curves mark the surfaces derived from the same data by Law et al. (2021a). (*middle*) The $T_b(r)$ distributions (gray box-whisker plots; dispersions are small) extracted along those surfaces, compared with the adopted gas temperature models for those surfaces (red and orange curves) and the midplane (blue curve). The corresponding Law et al. (2021a) models are again shown as black curves. While not used directly here, the extracted $T_b(r)$ distributions for the MAPS C^{18}O $J=2-1$ data (assuming it originates in the midplane) are also shown for reference (light gray circles). (*bottom*) The median temperature distribution from the reconstruction adopted based on interpolation of the information in the top two panels, with the same scale and annotations as in Figure 2.

presented in Appendix B. We adopted $\Delta x = 5 \pm 7$ mas, $\Delta y = 1 \pm 7$ mas, $i = -36^\circ.3 \pm 0^\circ.5$, $\vartheta = 327^\circ.7 \pm 0^\circ.7$, and

$v_{\text{sys}} = 5100 \pm 10$ m s $^{-1}$ (assuming $d = 162$ pc; Gaia Collaboration et al. 2023). The Layer 2 extractions and inferences were performed as described in Section 4.2 for ^{12}CO and ^{13}CO separately (using the same Layer 1 draws). The results are shown together in Figure 24: the inferred emission surfaces are comparable to those found by Law et al. (2021a).

The brightness temperature profiles extracted along those surfaces in Layer 3 are also shown in Figure 24 (as was also seen in Figure 18, the T_b dispersions are small). We were unable to find a two-dimensional temperature prescription that satisfactorily accounts for these profiles. For reference, the Law et al. (2021a) best-fit model profiles are overlaid as well, and it is apparent that they have substantial deviations (particularly at larger r) indicative of an imperfect model prescription. Until some insights on a more flexible $T(r, z)$ parameterization are available (a weakness we noted in Section 6.2), we opted for a modified approach. For each $\{\theta_1, \theta_2\}$ draw, we fit exponentially tapered power-law temperature profiles to the extracted $T_b(r)$ along the surface for each line and adopted the midplane temperature profile derived by Zhang et al. (2021) (as approximated with uncertainties by Sierra et al. 2021): the medians for each of those three profiles are marked in the middle panel of Figure 24. The $T(r, z)$ distribution was then approximated using bilinear interpolation between those three layers, assuming the vertical temperature profile saturates (becomes constant) above the ^{12}CO surface. The median $T(r, z)$ approximated in this way in Layer 3 is shown in the bottom panel of Figure 24.

The velocity profiles for each of 1,000 $\{\theta_1, \theta_2\}$ draws were extracted for both the ^{12}CO and ^{13}CO lines as described in Section 4.4. These profiles were then corrected at smaller r following the procedure detailed in Section 5.1, again using mock cubes generated with `csalt`: the correction factors $\mathcal{C}_v(r)$ are similar to those shown in Figure 13. We set the annular spacing of these extractions to $0''.05$, and limited consideration to the ranges $r < 600$ and 400 au for ^{12}CO and ^{13}CO , respectively, based on the behaviors of their surfaces and $T_b(r)$ (Figure 24). Using draws from the $T(r, z)$ prescription described above, we then performed the Layer 4 inference for *both lines* jointly (using the sum of log-likelihoods for ^{12}CO and ^{13}CO lines as a composite log-likelihood). The only other modification from the procedure outlined in Section 5.3 was to adjust the soft upper boundary of the r_t prior (Eq. 37) from 300 to 600 au, to accommodate the larger extent of the MWC 480 disk.

The inferred θ_4 covariances and marginalized posterior distributions are shown in Figure 25 (autocorrelation times were ~ 150 steps). As before, we also show comparisons between the extracted $\Delta v_\phi(r)$ distributions and models reconstructed from posterior draws. In this case (since we do not know v_*), we defined the residual velocity profiles with respect to the v_* evaluated at the best-fit (peak of the marginal posteriors) for M_* and the

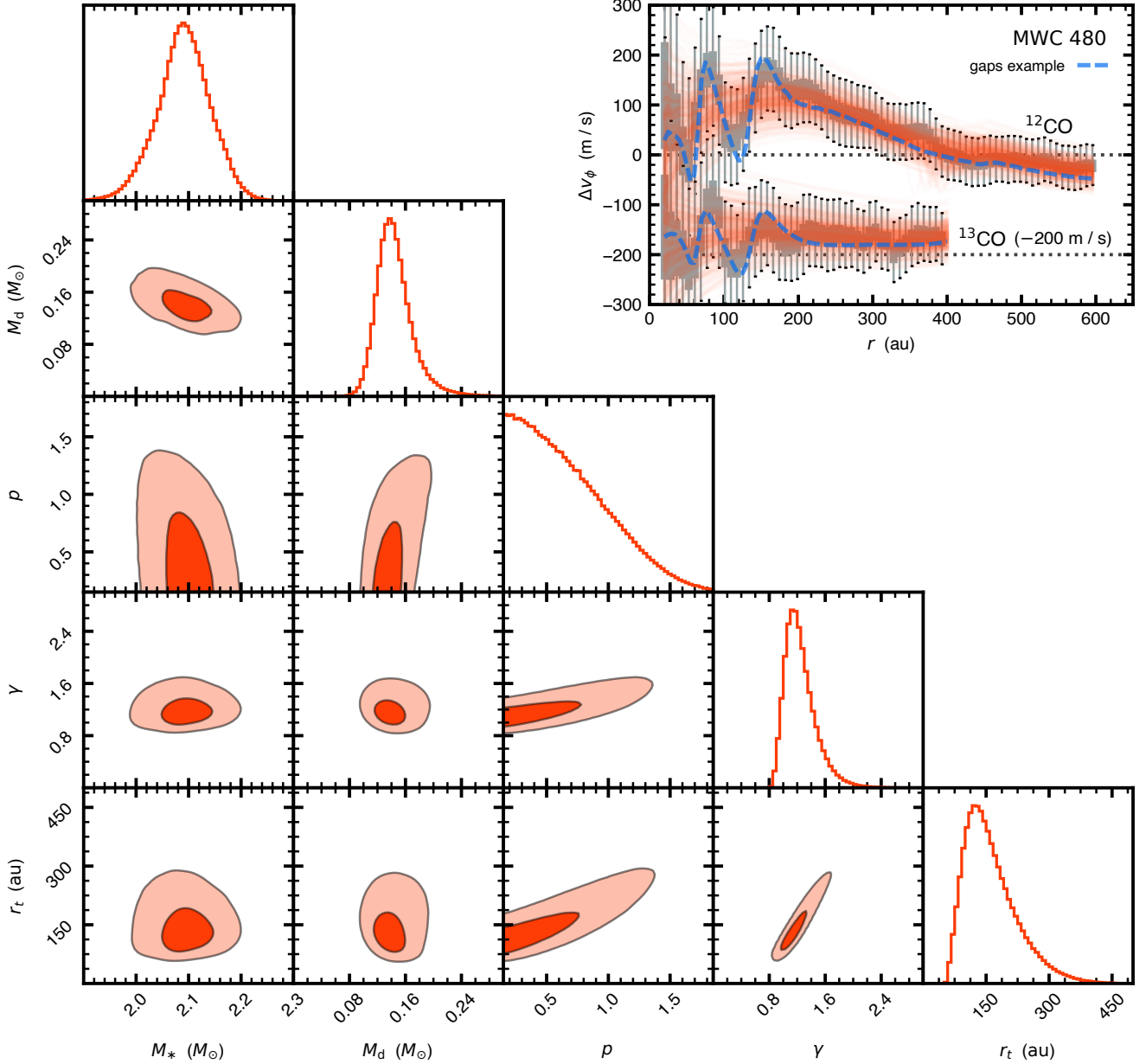


Figure 25. The marginalized θ_4 posteriors for the joint inference of the ^{12}CO and ^{13}CO kinematics in the MWC 480 disk: contours mark the 1 and 2σ confidence intervals (see Table 3). The panel in the upper right shows binned summaries of the extracted (residual) velocity profile data, compared with the reconstructed Δv_m from 1,000 draws of the θ_4 posteriors. Here, the residual profiles are defined with reference to the best-fit v_* for each line. Note that the ^{13}CO extractions and models have been offset lower by 200 m s^{-1} for clarity (as marked by the second horizontal dotted line). The dashed blue curves show an example variant of the best-fit model that imposes two gaps on the baseline surface density profile, to demonstrate that such substructures can account for the kinematic oscillations found within $r \approx 150 \text{ au}$ without introducing any significant bias.

posterior medians of θ_2 for each line: note that the ^{13}CO data and models have been offset (lower by 200 m s^{-1}) to minimize overlap for the sake of clarity. Summaries of these inferences are provided in Table 3.

Overall, the quality and general behavior of these posterior inferences are quite similar to those determined in the controlled injection/recovery experiments described

in Section 5 for similarly massive disks, particularly when considering that the MWC 480 disk is larger (more radial dynamic range is available) and we have combined two spectral line tracers. For reference, we inferred a mass ratio $M_d/M_* = 7 \pm 1\%$ in this case, consistent with expectations based on a comparison with Figure 23. We should also note that inferences using only the ^{12}CO or

Table 3. Inferred MWC 480 Parameters

M_* (M_\odot)	M_d (M_\odot)	p	γ	r_t (au)
2.09 ^{+0.06} _{-0.04}	0.13 ^{+0.04} _{-0.01}	0.5 ^{+0.5} _{-0.4}	1.1 ^{+0.3} _{-0.1}	124 ⁺⁹⁹ ₋₂₁

NOTE—Uncertainties represent the 68.3% (1σ) confidence intervals. Note that the p inference is formally consistent with the assumed prior (Eq. 37).

^{13}CO data alone are consistent with the joint inference, albeit with poorer precision and relatively small biases (the ^{13}CO data alone are essentially insensitive to r_t , and thereby p and γ , in part due to the limited spatial dynamic range and v_ϕ precision).

But despite the general quality of the inferences in this case, the simple prescriptions for the physical parameters that we have adopted are unable to explain a variety of details in the observed quantities. Specifically, there are clear, smaller-scale “oscillations” in the line emission distributions throughout the MWC 480 disk, identifiable in the extracted profiles for the emission surfaces, brightness temperatures, and velocities (Law et al. 2021a,b; Teague et al. 2021; Figures 24 and 25). While it is not clear what physical mechanisms produce these features, they are presumably indications of localized substructures in the physical conditions and/or dynamics. The focus here is not in accounting for these features by significantly expanding the model prescription(s), but it is worth considering how these substructures might bias the simplistic $\Sigma(r)$ inferences described above.

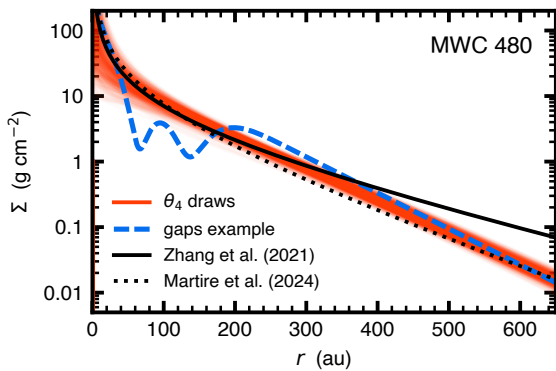


Figure 26. The surface density profiles reconstructed from random draws of the θ_4 posteriors for the joint fit of the ^{12}CO and ^{13}CO kinematics in the MWC 480 disk, along with the example model that was manually tuned with Gaussian gaps to reproduce the kinematic substructures. These profiles are compared with the $\Sigma(r)$ derived by Martire et al. (2024) for a similar kinematic analysis (but with fixed p and γ), and by Zhang et al. (2021) from independent, complementary thermo-chemical modeling of continuum and spectral line (CO isotopologue) intensities.

An inspection of the residual velocity profiles in Figure 25 suggest that the most significant concerns along these lines are the strong ($\pm 100 \text{ m s}^{-1}$) kinematic oscillations present for both spectral lines inside $r \approx 150 \text{ au}$. If those oscillations are intrinsically asymmetric enough (in amplitude) that the smooth model prescriptions we adopted do not recover well the mean behavior of the underlying profiles, we could expect these substructures to induce a bias in the M_*-M_d degeneracy that has characteristics similar to the resolution problem described in Section 5.1. As a test to guide expectations, we considered a simplistic modification of the smooth $\Sigma(r)$ in Eq. (9) that imparts these kinds of kinematic oscillations through (primarily) the associated pressure modulations (i.e., manifested through ε_p). This involved introducing two gaps in the baseline $\Sigma(r)$ structure (Table 3), centered at 65 and 135 au with Gaussian widths (standard deviations) and (fractional) depletions of 30 and 40 au and 94 and 88%, respectively. Those simple, manually tuned features generate kinematic oscillations that reproduce quite well the extracted Δv_ϕ profiles, as shown by the dashed blue curves in Figure 25. This match suggests that these substructures are not a source of significant bias here: the constraints on $\Sigma(r)$ are dominated by the self-gravity contributions at larger r .

Figure 26 shows the $\Sigma(r)$ profiles reconstructed from random draws of the θ_4 posteriors (as shown in Figure 25) and this example model with localized density gaps. Overlaid are the $\Sigma(r)$ estimates from Martire et al. (2024), based on a similar kinematic analysis (but with fixed density gradients $p = \gamma = 1$), and Zhang et al. (2021), derived from detailed thermo-chemical modeling based on the emission intensities from the dust continuum and CO isotopologue spectral lines. The general agreement between these independent techniques is striking, particularly when considering that Zhang et al. (2021) relied on extrapolation beyond $\sim 400 \text{ au}$ where the CO isotopologue (and dust continuum) emission is unavailable. This consistency again points to opportunity for future work, where leveraging both approaches together could offer an even more robust approach for constraining the physical conditions in these gas disks.

Even though the example model $\Sigma(r)$ with gaps is not an optimized or unique solution, it is worth noting that the behavior it predicts is also generally consistent with other available diagnostics. For example, the $\sim 65 \text{ au}$ ($0''.4$) gap and corresponding 100 au ($0''.6$) peak are also seen as analogous substructures in the millimeter continuum (Long et al. 2018; Liu et al. 2019; Sierra et al. 2021) and various other emission lines (Law et al. 2021b; e.g., the ^{13}CO and C^{18}O profiles shown in Figure 24). This suggests there are exciting opportunities to better leverage these kinematic deviations with various intensity tracers to quantify the physical conditions associated with substructures, and particularly for characterizing localized pressure maxima and particle traps (e.g., Rosotti et al. 2020; Yen & Gu 2020).

7. SUMMARY

We conducted a methodological study for a technique that relies on kinematic information from resolved spectral line observations to measure the mass and density distribution of a protoplanetary gas disk. We found:

- A layered analysis framework that sequentially extracts information from the observations and estimates relevant parameters can be used to effectively propagate uncertainties in the disk geometry, emission surface location, and physical conditions into inferences of the density distribution;
- The quality of constraints on M_d are most significantly affected by the ambiguities (degeneracies) in the shape of the surface density profile – especially the taper at large r – and the quality of estimates for extrinsic (geometric) parameters;
- For sensitive data with sufficiently high resolution, and adopting reasonable priors, we can recover $\Sigma(r)$ with remarkable fidelity for massive disks ($M_d/M_* \gtrsim 5\%$) using only the kinematic information from a single spectral line. The M_d precision could potentially be improved with some tool refinements and by combining tracers.
- We illustrated this approach using archival ALMA observations of the MWC 480 disk, inferring a gas mass ($M_d = 0.13^{+0.04}_{-0.01} M_\odot$, or $M_d/M_* = 7 \pm 1\%$) and surface density profile in good agreement with a thermo-chemical modeling analysis of the spectral line and continuum intensities by Zhang et al. (2021). We also demonstrated that conspicuous kinematics features could be explained with localized density depletions at 65 and 135 au (and a corresponding pressure maximum around 100 au), consistent with the substructures identified in other (intensity-based) tracers.

While the effects are subtle and observations are challenging, this approach for dynamical estimates of protoplanetary disk masses – particularly at the higher end of the mass distribution, where intensity-based approaches will struggle with optical depth effects – should have an especially promising future role in expanding our quantitative understanding of the planet formation process.

ACKNOWLEDGMENTS

We are grateful to Cristiano Longarini, Kees Dullemond, David Wilner, and Christophe Pinte for their thoughtful suggestions, to Sylvain Kozzennik for his patient advice on computing, and to Feng Long and Anibal Sierra for sharing results. We acknowledge an exceptionally helpful report from an anonymous reviewer. Some of the computations used in this research were conducted on the Smithsonian High Performance Cluster (SI/HPC), Smithsonian Institution (<https://doi.org/10.25572/SI/HP>). S.A. acknowledges support from the National Aeronautics and Space Administration under grant 17-XRP17_2-0012 issued through the Exoplanets Research Program.

This paper makes use of the following ALMA data: ADS/JAO.ALMA#2018.1.01055.L. ALMA is a partnership of ESO (representing its member states), NSF (USA) and NINS (Japan), together with NRC (Canada), MOST and ASIAA (Taiwan), and KASI (Republic of Korea), in cooperation with the Republic of Chile. The Joint ALMA Observatory is operated by ESO, AUI/NRAO and NAOJ. The National Radio Astronomy Observatory is a facility of the National Science Foundation operated under cooperative agreement by Associated Universities, Inc.

Software:

`analysisUtils` (Hunter et al. 2023), `astropy` (Astropy Collaboration et al. 2022, 2018, 2013), `bettermoments` (Teague & Foreman-Mackey 2018; Teague 2019), `CASA` (CASA Team et al. 2022), `cmasher` (van der Velden 2020), `corner` (Foreman-Mackey 2016), `csalt` (Andrews et al., *in preparation*)², `disksurf` (Teague et al. 2021), `eddy` (Teague 2019b), `emcee` (Foreman-Mackey et al. 2013), `frank` (Jennings et al. 2020), `gofish` (Teague 2019a), `numpy` (Harris et al. 2020), `matplotlib` (Hunter 2007), `RADMC-3D` (Dullemond et al. 2012), `vis_sample` (Loomis et al. 2018)³.

² <https://github.com/seanandrews/csalt>

³ https://github.com/AstroChem/vis_sample

APPENDIX

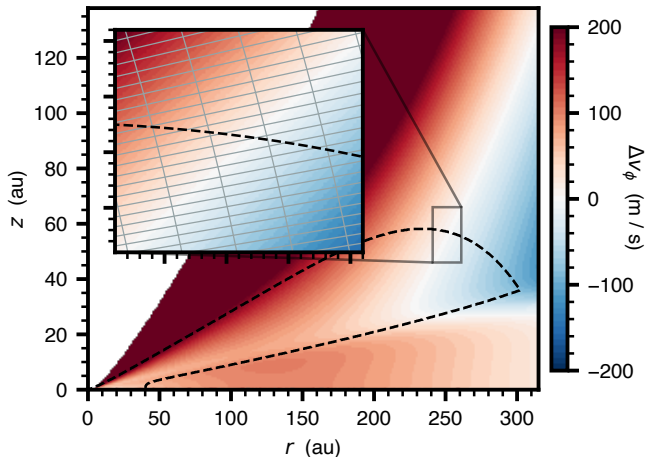


Figure 27. The main panel shows the same velocity residuals map for **model B** as in Figure 4 (bottom row, middle column), although over a slightly extended vertical domain. The inset panel shows a small subset of that distribution with the locations of the RADMC-3D grid cells (spherical coordinates) overlaid. The inset is shown with equal aspect ratio in cylindrical coordinates, with a Δv_ϕ colorscale condensed by a factor of 5 compared to the main panel (i.e., the full colorscale represents $\pm 40 \text{ m s}^{-1}$) for clarity. This example illustrates that the radiative transfer grid samples well the physical properties of the model near the top of the CO-rich layer, where most of the line emission is generated.

A. NOTES ON THE MODEL GRIDDING

In generating synthetic datasets using RADMC-3D as described in Section 3.1, the physical conditions, kinematics, and molecular abundances for a given model were specified on a fixed grid in spherical coordinates (R, Θ) . Here $R = \sqrt{r^2 + z^2}$ is the distance from the origin (stellar position), and $\Theta = \arctan(r/z)$ is the polar angle (such that $\Theta = \pi/2$ is the midplane). This coordinate frame has distinct numerical advantages for flared disk geometries, since it effectively has a built-in refinement to cover an appropriate dynamic range in height at all radii. That said, it can be somewhat clumsy for defining physical structures (see below). We defined the grid to have 360 cells in the R dimension, distributed logarithmically from 1 to 500 au. In the polar angle dimension, we distributed 240 cells logarithmically from the midplane (denser) to the pole (sparser). Figure 27 shows an example of the grid sampling for the **model B** velocity residuals, demonstrating that the physical properties are well-sampled in the relevant model regions.

Some attributes of a model can be directly calculated on this grid, simply using the $(r, z) \rightarrow (R, \Theta)$ mapping (e.g., T or v_*). However, for other quantities that rely

on integrals in cylindrical coordinates (e.g., ρ or ε_g), we computed a refined (one-dimensional) subgrid in cylindrical coordinates around each cell in the RADMC-3D grid. This is notably inefficient, but it ensured that numerical artifacts from interpolation methods did not introduce any undesired bias into the synthetic data products (and we only needed to compute a small number of datasets for the purposes of this article). Some testing verified that the pressure gradient in the ε_p kinematic deviation (Eq. 10) could be calculated in a straightforward way (once ρ was determined), using the chain rule,

$$\frac{\partial P}{\partial r} = \frac{\partial P}{\partial R} \sin \Theta + \frac{1}{R} \frac{\partial P}{\partial \Theta} \cos \Theta, \quad (\text{A1})$$

without resorting to another subgrid calculation.

B. MWC 480 GEOMETRIC PARAMETERS

For the analysis described in Section 6.3, we derived the geometric parameters in **Layer 1** from the visibility measurements of the $\sim 225 \text{ GHz}$ continuum associated with the same (^{12}CO and ^{13}CO) spectral line observations (Öberg et al. 2021). Because those data share the same calibration procedure, their relative offsets from the phase center (Δx and Δy) must be the same. Presuming there is no warp or large-scale axisymmetry, the projection angles (i and ϑ) should also be the same. We followed the procedure outlined by Andrews et al. (2021). To briefly summarize, for a given choice of $\{\Delta x, \Delta y, i, \vartheta\}$ we deprojected the continuum visibilities and modeled them assuming axisymmetry with the **frank** package (Jennings et al. 2020). That process was iterated for different geometries until we reached a satisfactory map that minimized the imaged residual visibilities. Figure 28 shows the images generated from the data, an optimized model, and the corresponding residual visibilities on the same spatial and intensity scales.

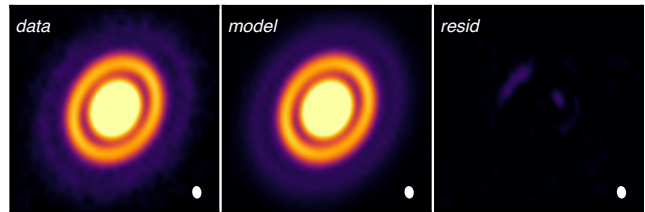


Figure 28. The images synthesized from the observed 225 GHz continuum visibilities for the MWC 480 disk (*left*), the best-fit **frank** model (*middle*), and the associated residuals (*right*) on the same spatial (425 au on a side) and intensity (an **asinh** brightness temperature stretch from 0 to 5 K) scales. The synthesized beam dimensions ($0''.16 \times 0''.11$) are shown in the lower right corners of each panel.

The **Layer 1** extractions assumed uncertainties based on a qualitative assessment of the outcomes of this procedure over a modest-sized grid of geometric parameters. Figure 29 illustrates the estimated uncertainties in terms of the imaged residuals (here in S/N units, with respect to the mean RMS noise value of $31 \mu\text{Jy beam}^{-1}$) for positive and negative variations of each parameter around the adopted values, with all other geometric parameters fixed. The bright, centrally peaked emission distribution means that the formal precision of the offset parameters, Δx and Δy , is especially high: the residuals are notably stronger for deviations of only ~ 1 mas in either dimension. However, we conservatively inflated the adopted uncertainties (to ± 7 mas) because of the lingering asymmetric residuals we find even in the optimized case. The inclination and position angle variations are more subtle, but still exhibit the distinctive patterns in the residual images noted by Andrews et al. (2021). Even for our best estimates, there are substantial residuals. The strongest of these are primarily associated with the bright emission ring along the minor axis, consistent with expectations for an elevated (and presumably optically thick) emission surface.

The adopted geometry is similar to those estimated by Teague et al. (2021) and Izquierdo et al. (2023) from the same data. We found i closer to the latter estimates based on the rare isotopologues, and consistent ϑ . But quantitatively, the offsets are demonstrably different compared to both studies (and as noted above, are constrained well): even though the shifts are still well within the size of the synthesized beam, these differences can have non-trivial effects on the velocity extractions. As noted above, this can be one of the important systematic limitation for kinematic studies.

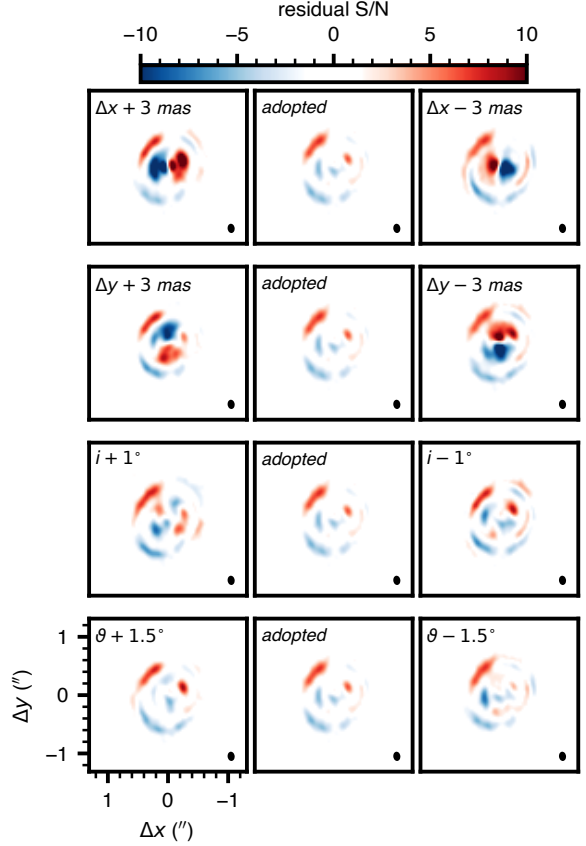


Figure 29. The images synthesized from the residual 225 GHz continuum visibilities for the MWC 480 disk for the adopted geometry – with $\Delta x = 5$ mas, $\Delta y = 1$ mas, $i = -36^\circ.3$, $\vartheta = 327^\circ.7$ – are shown in the middle column (same for all rows). Each row compares a variation in a single parameter, as annotated. The offsets introduce strong residuals (here showing only half the standard deviation adopted in the inferences), while the projection angles have more subtle effects (the i and ϑ ranges are $\pm 2\sigma$ for the adopted ranges). All plots are shown on the same spatial scale (as in Figure 28) and using a linear stretch of the residual S/N (normalized by the RMS = $31 \mu\text{Jy beam}^{-1}$). The beam dimensions are marked in the lower right of each panel.

REFERENCES

- Aikawa, Y., Miyama, S. M., Nakano, T., & Umebayashi, T. 1996, *ApJ*, 467, 684, doi: [10.1086/177644](https://doi.org/10.1086/177644)
- Aikawa, Y., & Nomura, H. 2006, *ApJ*, 642, 1152, doi: [10.1086/501114](https://doi.org/10.1086/501114)
- Aikawa, Y., van Zadelhoff, G. J., van Dishoeck, E. F., & Herbst, E. 2002, *A&A*, 386, 622, doi: [10.1051/0004-6361:20020037](https://doi.org/10.1051/0004-6361:20020037)
- Alcalá, J. M., Manara, C. F., Natta, A., et al. 2017, *A&A*, 600, A20, doi: [10.1051/0004-6361/201629929](https://doi.org/10.1051/0004-6361/201629929)
- ALMA Partnership, Brogan, C. L., Pérez, L. M., et al. 2015, *ApJL*, 808, L3, doi: [10.1088/2041-8205/808/1/L3](https://doi.org/10.1088/2041-8205/808/1/L3)
- Anderson, D. E., Blake, G. A., Bergin, E. A., et al. 2019, *ApJ*, 881, 127, doi: [10.3847/1538-4357/ab2cb5](https://doi.org/10.3847/1538-4357/ab2cb5)
- Anderson, D. E., Cleeves, L. I., Blake, G. A., et al. 2022, *ApJ*, 927, 229, doi: [10.3847/1538-4357/ac517e](https://doi.org/10.3847/1538-4357/ac517e)
- Andrews, S. M. 2020, *ARA&A*, 58, 483, doi: [10.1146/annurev-astro-031220-010302](https://doi.org/10.1146/annurev-astro-031220-010302)
- Andrews, S. M., & Williams, J. P. 2005, *ApJ*, 631, 1134, doi: [10.1086/432712](https://doi.org/10.1086/432712)
- Andrews, S. M., Wilner, D. J., Zhu, Z., et al. 2016, *ApJL*, 820, L40, doi: [10.3847/2041-8205/820/2/L40](https://doi.org/10.3847/2041-8205/820/2/L40)
- Andrews, S. M., Huang, J., Pérez, L. M., et al. 2018, *ApJL*, 869, L41, doi: [10.3847/2041-8213/aaf741](https://doi.org/10.3847/2041-8213/aaf741)
- Andrews, S. M., Elder, W., Zhang, S., et al. 2021, *ApJ*, 916, 51, doi: [10.3847/1538-4357/ac00b9](https://doi.org/10.3847/1538-4357/ac00b9)
- Armitage, P. J. 2010, *Astrophysics of Planet Formation*
- Astropy Collaboration, Robitaille, T. P., Tollerud, E. J., et al. 2013, *A&A*, 558, A33, doi: [10.1051/0004-6361/201322068](https://doi.org/10.1051/0004-6361/201322068)
- Astropy Collaboration, Price-Whelan, A. M., Sipőcz, B. M., et al. 2018, *AJ*, 156, 123, doi: [10.3847/1538-3881/aabc4f](https://doi.org/10.3847/1538-3881/aabc4f)
- Astropy Collaboration, Price-Whelan, A. M., Lim, P. L., et al. 2022, *ApJ*, 935, 167, doi: [10.3847/1538-4357/ac7c74](https://doi.org/10.3847/1538-4357/ac7c74)
- Baraffe, I., Homeier, D., Allard, F., & Chabrier, G. 2015, *A&A*, 577, A42, doi: [10.1051/0004-6361/201425481](https://doi.org/10.1051/0004-6361/201425481)
- Beckwith, S. V. W., Sargent, A. I., Chini, R. S., & Guesten, R. 1990, *AJ*, 99, 924, doi: [10.1086/115385](https://doi.org/10.1086/115385)
- Bergin, E. A., & Williams, J. P. 2018, arXiv e-prints, arXiv:1807.09631. <https://arxiv.org/abs/1807.09631>
- Bergin, E. A., Cleeves, L. I., Gorti, U., et al. 2013, *Nature*, 493, 644, doi: [10.1038/nature11805](https://doi.org/10.1038/nature11805)
- Bertin, G., & Lodato, G. 1999, *A&A*, 350, 694. <https://arxiv.org/abs/astro-ph/9908095>
- Birnstiel, T., Fang, M., & Johansen, A. 2016, *SSRv*, 205, 41, doi: [10.1007/s11214-016-0256-1](https://doi.org/10.1007/s11214-016-0256-1)
- Birnstiel, T., Klahr, H., & Ercolano, B. 2012, *A&A*, 539, A148, doi: [10.1051/0004-6361/201118136](https://doi.org/10.1051/0004-6361/201118136)
- Birnstiel, T., Dullemond, C. P., Zhu, Z., et al. 2018, *ApJL*, 869, L45, doi: [10.3847/2041-8213/aaf743](https://doi.org/10.3847/2041-8213/aaf743)
- Boehler, Y., Ménard, F., Robert, C. M. T., et al. 2021, *A&A*, 650, A59, doi: [10.1051/0004-6361/202040089](https://doi.org/10.1051/0004-6361/202040089)
- Booth, A. S., Walsh, C., Ilee, J. D., et al. 2019, *ApJL*, 882, L31, doi: [10.3847/2041-8213/ab3645](https://doi.org/10.3847/2041-8213/ab3645)
- Carrasco-González, C., Sierra, A., Flock, M., et al. 2019, arXiv e-prints, arXiv:1908.07140. <https://arxiv.org/abs/1908.07140>
- CASA Team, Bean, B., Bhatnagar, S., et al. 2022, *PASP*, 134, 114501, doi: [10.1088/1538-3873/ac9642](https://doi.org/10.1088/1538-3873/ac9642)
- Casassus, S., Avenhaus, H., Pérez, S., et al. 2018, *MNRAS*, 477, 5104, doi: [10.1093/mnras/sty894](https://doi.org/10.1093/mnras/sty894)
- Chiang, E. I., & Goldreich, P. 1997, *ApJ*, 490, 368, doi: [10.1086/304869](https://doi.org/10.1086/304869)
- Cornwell, T. J. 2008, *IEEE Journal of Selected Topics in Signal Processing*, 2, 793, doi: [10.1109/JSTSP.2008.2006388](https://doi.org/10.1109/JSTSP.2008.2006388)
- D'Alessio, P., Calvet, N., Hartmann, L., Franco-Hernández, R., & Servín, H. 2006, *ApJ*, 638, 314, doi: [10.1086/498861](https://doi.org/10.1086/498861)
- de Boer, J., Salter, G., Benisty, M., et al. 2016, *A&A*, 595, A114, doi: [10.1051/0004-6361/201629267](https://doi.org/10.1051/0004-6361/201629267)
- Dullemond, C. P., Dominik, C., & Natta, A. 2001, *ApJ*, 560, 957, doi: [10.1086/323057](https://doi.org/10.1086/323057)
- Dullemond, C. P., Isella, A., Andrews, S. M., Skobleva, I., & Dzyurkevich, N. 2020, *A&A*, 633, A137, doi: [10.1051/0004-6361/201936438](https://doi.org/10.1051/0004-6361/201936438)
- Dullemond, C. P., Juhasz, A., Pohl, A., et al. 2012, *RADMC-3D: A multi-purpose radiative transfer tool*. <http://ascl.net/1202.015>
- Dutrey, A., Guilloteau, S., & Guelin, M. 1997, *A&A*, 317, L55
- Flaherty, K. M., Hughes, A. M., Teague, R., et al. 2018, *ApJ*, 856, 117, doi: [10.3847/1538-4357/aab615](https://doi.org/10.3847/1538-4357/aab615)
- Foreman-Mackey, D. 2016, *The Journal of Open Source Software*, 24, doi: [10.21105/joss.00024](https://doi.org/10.21105/joss.00024)
- Foreman-Mackey, D., Hogg, D. W., Lang, D., & Goodman, J. 2013, *PASP*, 125, 306, doi: [10.1086/670067](https://doi.org/10.1086/670067)
- Gaia Collaboration, Vallenari, A., Brown, A. G. A., et al. 2023, *A&A*, 674, A1, doi: [10.1051/0004-6361/202243940](https://doi.org/10.1051/0004-6361/202243940)
- Galloway-Sprietsma, M., Bae, J., Teague, R., et al. 2023, *ApJ*, 950, 147, doi: [10.3847/1538-4357/accae4](https://doi.org/10.3847/1538-4357/accae4)
- Harris, C. R., Millman, K. J., van der Walt, S. J., et al. 2020, *Nature*, 585, 357, doi: [10.1038/s41586-020-2649-2](https://doi.org/10.1038/s41586-020-2649-2)
- Hirose, S., & Turner, N. J. 2011, *ApJL*, 732, L30, doi: [10.1088/2041-8205/732/2/L30](https://doi.org/10.1088/2041-8205/732/2/L30)
- Huang, J., Andrews, S. M., Cleeves, L. I., et al. 2018a, *ApJ*, 852, 122, doi: [10.3847/1538-4357/aaa1e7](https://doi.org/10.3847/1538-4357/aaa1e7)
- Huang, J., Andrews, S. M., Dullemond, C. P., et al. 2018b, *ApJL*, 869, L42, doi: [10.3847/2041-8213/aaf740](https://doi.org/10.3847/2041-8213/aaf740)

- Hunter, J. D. 2007, *Computing In Science & Engineering*, 9, 90
- Hunter, T. R., Petry, D., Barkats, D., Corder, S., & Indebetouw, R. 2023, *analysisUtils*, 2.90, Zenodo, Zenodo, doi: [10.5281/zenodo.8408419](https://doi.org/10.5281/zenodo.8408419)
- Izquierdo, A. F., Testi, L., Facchini, S., Rosotti, G. P., & van Dishoeck, E. F. 2021, *A&A*, 650, A179, doi: [10.1051/0004-6361/202140779](https://doi.org/10.1051/0004-6361/202140779)
- Izquierdo, A. F., Testi, L., Facchini, S., et al. 2023, *A&A*, 674, A113, doi: [10.1051/0004-6361/202245425](https://doi.org/10.1051/0004-6361/202245425)
- Jennings, J., Booth, R. A., Tazzari, M., Rosotti, G. P., & Clarke, C. J. 2020, *MNRAS*, 495, 3209, doi: [10.1093/mnras/staa1365](https://doi.org/10.1093/mnras/staa1365)
- Keppler, M., Teague, R., Bae, J., et al. 2019, *A&A*, 625, A118, doi: [10.1051/0004-6361/201935034](https://doi.org/10.1051/0004-6361/201935034)
- Krijt, S., Bosman, A. D., Zhang, K., et al. 2020, *ApJ*, 899, 134, doi: [10.3847/1538-4357/aba75d](https://doi.org/10.3847/1538-4357/aba75d)
- Law, C., Furuya, K., Loomis, R., et al. 2020, *ApJ*, 810, 112, doi: [10.1088/0004-637X/810/2/112](https://doi.org/10.1088/0004-637X/810/2/112)
- Law, C. J., Teague, R., Loomis, R. A., et al. 2021a, *ApJS*, 257, 4, doi: [10.3847/1538-4365/ac1439](https://doi.org/10.3847/1538-4365/ac1439)
- Law, C. J., Loomis, R. A., Teague, R., et al. 2021b, *ApJS*, 257, 3, doi: [10.3847/1538-4365/ac1434](https://doi.org/10.3847/1538-4365/ac1434)
- Law, C. J., Crystian, S., Teague, R., et al. 2022, *ApJ*, 932, 114, doi: [10.3847/1538-4357/ac6c02](https://doi.org/10.3847/1538-4357/ac6c02)
- Liu, Y., Dipierro, G., Ragusa, E., et al. 2019, *A&A*, 622, A75, doi: [10.1051/0004-6361/201834157](https://doi.org/10.1051/0004-6361/201834157)
- Liu, Y., Linz, H., Fang, M., et al. 2022, *A&A*, 668, A175, doi: [10.1051/0004-6361/202244505](https://doi.org/10.1051/0004-6361/202244505)
- Lodato, G., Rampinelli, L., Viscardi, E., et al. 2023, *MNRAS*, 518, 4481, doi: [10.1093/mnras/stac3223](https://doi.org/10.1093/mnras/stac3223)
- Long, F., Pinilla, P., Herczeg, G. J., et al. 2018, *ApJ*, 869, 17, doi: [10.3847/1538-4357/aae8e1](https://doi.org/10.3847/1538-4357/aae8e1)
- Long, F., Andrews, S. M., Rosotti, G., et al. 2022, *ApJ*, 931, 6, doi: [10.3847/1538-4357/ac634e](https://doi.org/10.3847/1538-4357/ac634e)
- Loomis, R. A., Öberg, K. I., Andrews, S. M., et al. 2018, *AJ*, 155, 182, doi: [10.3847/1538-3881/aab604](https://doi.org/10.3847/1538-3881/aab604)
- Lynden-Bell, D., & Pringle, J. E. 1974, *MNRAS*, 168, 603
- Macías, E., Guerra-Alvarado, O., Carrasco-González, C., et al. 2021, *A&A*, 648, A33, doi: [10.1051/0004-6361/202039812](https://doi.org/10.1051/0004-6361/202039812)
- Martire, P., Longarini, C., Lodato, G., et al. 2024, *arXiv e-prints*, arXiv:2402.12236, doi: [10.48550/arXiv.2402.12236](https://doi.org/10.48550/arXiv.2402.12236)
- McClure, M. K., Bergin, E. A., Cleeves, L. I., et al. 2016, *ApJ*, 831, 167, doi: [10.3847/0004-637X/831/2/167](https://doi.org/10.3847/0004-637X/831/2/167)
- Miotello, A., Bruderer, S., & van Dishoeck, E. F. 2014, *A&A*, 572, A96, doi: [10.1051/0004-6361/201424712](https://doi.org/10.1051/0004-6361/201424712)
- Miotello, A., Kamp, I., Birnstiel, T., Cleeves, L. C., & Kataoka, A. 2023, *ASP Conference Series, Protostars and Planets VII*, 534, 501, doi: [10.48550/arXiv.2203.09818](https://doi.org/10.48550/arXiv.2203.09818)
- Miotello, A., van Dishoeck, E. F., Kama, M., & Bruderer, S. 2016, *A&A*, 594, A85, doi: [10.1051/0004-6361/201628159](https://doi.org/10.1051/0004-6361/201628159)
- Miotello, A., van Dishoeck, E. F., Williams, J. P., et al. 2017, *A&A*, 599, A113, doi: [10.1051/0004-6361/201629556](https://doi.org/10.1051/0004-6361/201629556)
- Molyarova, T., Akimkin, V., Semenov, D., et al. 2017, *ApJ*, 849, 130, doi: [10.3847/1538-4357/aa9227](https://doi.org/10.3847/1538-4357/aa9227)
- Öberg, K. I., Guzmán, V. V., Walsh, C., et al. 2021, *ApJS*, 257, 1, doi: [10.3847/1538-4365/ac1432](https://doi.org/10.3847/1538-4365/ac1432)
- Ossenkopf, V., & Henning, T. 1994, *A&A*, 291, 943
- Paneque-Carreño, T., Miotello, A., van Dishoeck, E. F., et al. 2023, *A&A*, 669, A126, doi: [10.1051/0004-6361/202244428](https://doi.org/10.1051/0004-6361/202244428)
- Pérez, S., Dunhill, A., Casassus, S., et al. 2015, *ApJL*, 811, L5, doi: [10.1088/2041-8205/811/1/L5](https://doi.org/10.1088/2041-8205/811/1/L5)
- Pinte, C., Teague, R., Flaherty, K., et al. 2023, *ASP Conference Series, Protostars and Planets VII*, 534, 645, doi: [10.48550/arXiv.2203.09528](https://doi.org/10.48550/arXiv.2203.09528)
- Pinte, C., Ménard, F., Duchêne, G., et al. 2018, *A&A*, 609, A47, doi: [10.1051/0004-6361/201731377](https://doi.org/10.1051/0004-6361/201731377)
- Qi, C., Wilner, D. J., Aikawa, Y., Blake, G. A., & Hogerheijde, M. R. 2008, *ApJ*, 681, 1396, doi: [10.1086/588516](https://doi.org/10.1086/588516)
- Ricci, L., Trotta, F., Testi, L., et al. 2012, *A&A*, 540, A6, doi: [10.1051/0004-6361/201118296](https://doi.org/10.1051/0004-6361/201118296)
- Rich, E. A., Teague, R., Monnier, J. D., et al. 2021, *ApJ*, 913, 138, doi: [10.3847/1538-4357/abf92e](https://doi.org/10.3847/1538-4357/abf92e)
- Rosenfeld, K. A., Andrews, S. M., Hughes, A. M., Wilner, D. J., & Qi, C. 2013, *ApJ*, 774, 16, doi: [10.1088/0004-637X/774/1/16](https://doi.org/10.1088/0004-637X/774/1/16)
- Rosenfeld, K. A., Chiang, E., & Andrews, S. M. 2014, *ApJ*, 782, 62, doi: [10.1088/0004-637X/782/2/62](https://doi.org/10.1088/0004-637X/782/2/62)
- Rosenfeld, K. A., Qi, C., Andrews, S. M., et al. 2012, *ApJ*, 757, 129, doi: [10.1088/0004-637X/757/2/129](https://doi.org/10.1088/0004-637X/757/2/129)
- Rosotti, G. P., Teague, R., Dullemond, C., Booth, R. A., & Clarke, C. J. 2020, *MNRAS*, 495, 173, doi: [10.1093/mnras/staa1170](https://doi.org/10.1093/mnras/staa1170)
- Sanchis, E., Testi, L., Natta, A., et al. 2021, *A&A*, 649, A19, doi: [10.1051/0004-6361/202039733](https://doi.org/10.1051/0004-6361/202039733)
- Schöier, F. L., van der Tak, F. F. S., van Dishoeck, E. F., & Black, J. H. 2005, *A&A*, 432, 369, doi: [10.1051/0004-6361:20041729](https://doi.org/10.1051/0004-6361:20041729)
- Schwarz, K. R., Bergin, E. A., Cleeves, L. I., et al. 2016, *ApJ*, 823, 91, doi: [10.3847/0004-637X/823/2/91](https://doi.org/10.3847/0004-637X/823/2/91)
- . 2018, *ApJ*, 856, 85, doi: [10.3847/1538-4357/aaae08](https://doi.org/10.3847/1538-4357/aaae08)
- Schwarz, K. R., Calahan, J. K., Zhang, K., et al. 2021, *ApJS*, 257, 20, doi: [10.3847/1538-4365/ac143b](https://doi.org/10.3847/1538-4365/ac143b)

- Sierra, A., Pérez, L. M., Zhang, K., et al. 2021, *ApJS*, 257, 14, doi: [10.3847/1538-4365/ac1431](https://doi.org/10.3847/1538-4365/ac1431)
- Teague, R. 2019, *Research Notes of the American Astronomical Society*, 3, 74, doi: [10.3847/2515-5172/ab2125](https://doi.org/10.3847/2515-5172/ab2125)
- Teague, R. 2019a, *The Journal of Open Source Software*, 4, 1632, doi: [10.21105/joss.01632](https://doi.org/10.21105/joss.01632)
- . 2019b, *The Journal of Open Source Software*, 4, 1220, doi: [10.21105/joss.01220](https://doi.org/10.21105/joss.01220)
- . 2020, *richteague/keplerian_mask*: Initial Release, 1.0, Zenodo, doi: [10.5281/zenodo.4321137](https://doi.org/10.5281/zenodo.4321137), <https://doi.org/10.5281/zenodo.4321137>
- Teague, R., Bae, J., Bergin, E. A., Birnstiel, T., & Foreman-Mackey, D. 2018, *ApJL*, 860, L12, doi: [10.3847/2041-8213/aac6d7](https://doi.org/10.3847/2041-8213/aac6d7)
- Teague, R., & Foreman-Mackey, D. 2018, *Research Notes of the American Astronomical Society*, 2, 173, doi: [10.3847/2515-5172/aae265](https://doi.org/10.3847/2515-5172/aae265)
- Teague, R., Law, C. J., Huang, J., & Meng, F. 2021, *Journal of Open Source Software*, 6, 3827, doi: [10.21105/joss.03827](https://doi.org/10.21105/joss.03827)
- Teague, R., Bae, J., Aikawa, Y., et al. 2021, *ApJS*, 257, 18, doi: [10.3847/1538-4365/ac1438](https://doi.org/10.3847/1538-4365/ac1438)
- Teague, R., Bae, J., Andrews, S. M., et al. 2022, *arXiv e-prints*, arXiv:2208.04837, <https://arxiv.org/abs/2208.04837>
- Testi, L., Birnstiel, T., Ricci, L., et al. 2014, *Protostars and Planets VI*, 339, doi: [10.2458/azu_uapress.9780816531240-ch015](https://doi.org/10.2458/azu_uapress.9780816531240-ch015)
- Toomre, A. 1964, *ApJ*, 139, 1217, doi: [10.1086/147861](https://doi.org/10.1086/147861)
- Trapman, L., Miotello, A., Kama, M., van Dishoeck, E. F., & Bruderer, S. 2017, *A&A*, 605, A69, doi: [10.1051/0004-6361/201630308](https://doi.org/10.1051/0004-6361/201630308)
- Trapman, L., Zhang, K., van't Hoff, M. L. R., Hogerheijde, M. R., & Bergin, E. A. 2022, *ApJL*, 926, L2, doi: [10.3847/2041-8213/ac4f47](https://doi.org/10.3847/2041-8213/ac4f47)
- van der Velden, E. 2020, *The Journal of Open Source Software*, 5, 2004, doi: [10.21105/joss.02004](https://doi.org/10.21105/joss.02004)
- van Zadelhoff, G.-J., Aikawa, Y., Hogerheijde, M. R., & van Dishoeck, E. F. 2003, *A&A*, 397, 789, doi: [10.1051/0004-6361:20021592](https://doi.org/10.1051/0004-6361:20021592)
- van Zadelhoff, G. J., van Dishoeck, E. F., Thi, W. F., & Blake, G. A. 2001, *A&A*, 377, 566, doi: [10.1051/0004-6361:20011137](https://doi.org/10.1051/0004-6361:20011137)
- Veronesi, B., Paneque-Carreño, T., Lodato, G., et al. 2021, *ApJL*, 914, L27, doi: [10.3847/2041-8213/abfe6a](https://doi.org/10.3847/2041-8213/abfe6a)
- Wang, L., Bai, X.-N., & Goodman, J. 2019, *ApJ*, 874, 90, doi: [10.3847/1538-4357/ab06fd](https://doi.org/10.3847/1538-4357/ab06fd)
- Williams, J. P., & Best, W. M. J. 2014, *ApJ*, 788, 59, doi: [10.1088/0004-637X/788/1/59](https://doi.org/10.1088/0004-637X/788/1/59)
- Yen, H.-W., & Gu, P.-G. 2020, *ApJ*, 905, 89, doi: [10.3847/1538-4357/abc55a](https://doi.org/10.3847/1538-4357/abc55a)
- Yu, M., Evans, II, N. J., Dodson-Robinson, S. E., Willacy, K., & Turner, N. J. 2017, *ApJ*, 841, 39, doi: [10.3847/1538-4357/aa6e4c](https://doi.org/10.3847/1538-4357/aa6e4c)
- Zhang, K., Bergin, E. A., Blake, G. A., Cleeves, L. I., & Schwarz, K. R. 2017, *Nature Astronomy*, 1, 0130, doi: [10.1038/s41550-017-0130](https://doi.org/10.1038/s41550-017-0130)
- Zhang, K., Booth, A. S., Law, C. J., et al. 2021, *ApJS*, 257, 5, doi: [10.3847/1538-4365/ac1580](https://doi.org/10.3847/1538-4365/ac1580)
- Zhu, Z., Zhang, S., Jiang, Y.-F., et al. 2019, *ApJL*, 877, L18, doi: [10.3847/2041-8213/ab1f8c](https://doi.org/10.3847/2041-8213/ab1f8c)